UC Riverside

UC Riverside Electronic Theses and Dissertations

Title
Path Planning for Autonomous Ground Vehicles using GNSS and Cellular LTE Signal
Reliability Maps and GIS 3-D Maps

Permalink
https://escholarship.org/uc/item/7pq5f4sc

Author
Ragothaman, Sonya

Publication Date
2018

Copyright Information

Peer reviewed|Thesis/dissertation

UNIVERSITY OF CALIFORNIA
RIVERSIDE

Path Planning for Autonomous Ground Vehicles using GNSS and Cellular LTE
Signal Reliability Maps and GIS 3-D Maps

A Thesis submitted in partial satisfaction
of the requirements for the degree of

Master of Science

in

Electrical Engineering

by

Sonya Shruthi Ragothaman

December 2018

Thesis Committee:

    Dr. Zaher (Zak) M. Kassas, Chairperson
    Dr. Jay A. Farrell
    Dr. Guoyuan Wu

The Thesis of Sonya Shruthi Ragothaman is approved:

_____

_____

_____
Committee Chairperson

University of California, Riverside

Acknowledgments

I am grateful to my advisor, Dr. Zak Kassas, who introduced me to this research topic and for pushing me to do my best. I'd like to thank him for giving me access to equipment to conduct experiments and to complete my masters. Although he was busy, I am grateful that he still made time to help me complete my journey at UCR. I would also like to thank Dr. Mahdi Maaref, who advised and taught me throughout my masters. His professionalism and patience as a mentor has inspired me. I am also grateful to my colleagues at ASPIN Lab, who have helped me throughout my journey. I am especially grateful to Joe Khalife from ASPIN Lab, who always had solid advice and suggestions which shaped my research.

I'm grateful to my boyfriend Cody, for reassuring me when needed, inspiring me to do my best, and helping me with my experiments. I'd also like to thank my friends, role models, and mentors that have shaped me throughout my youth, including Sundara Aunty, Jayashree Aunty, Yaamini, Sruti, Tiffany, and many more. They taught skills (e.g., persistence, attention to detail) which were useful for my research, and I would not be here without their support over the years. I would like to thank my friends throughout my graduate and undergraduate studies, including Jesse, Evan, Sanji, Tasnia, Charlene, Jose, and many others, who have made my experience at UCR unforgettably fun.

I would finally like to thank my family, Shobana, JB, and Kevin. They have always been encouraging and supportive of me, both financially and emotionally. They have taught me how to adapt to new situations and to be positive, which helped me throughout my journey at UCR. I would not be here without them, and I love them.

To my parents and brother.

ABSTRACT OF THE THESIS

Path Planning for Autonomous Ground Vehicles using GNSS and Cellular LTE Signal
Reliability Maps and GIS 3-D Maps

by

Sonya Shruthi Ragothaman

Master of Science, Graduate Program in Electrical Engineering
University of California, Riverside, December 2018
Dr. Zaher (Zak) M. Kassas, Chairperson

In this thesis, path planning for an autonomous ground vehicle (AGV) in an urban environment is considered. The following problem is considered. starting from an initial location, the AGV desires to reach a final location by taking the shortest distance, while minimizing the AGVs position estimation error and guaranteeing that the AGVs position estimation uncertainty is below a desired threshold. The AGV is assumed to be equipped with receivers capable of producing pseudodange measurements on Global Navigation Satellite System (GNSS) satellites and cellular long-term evolution (LTE) towers. Using a geographic information system (GIS) three-dimensional (3-D) building map building map of the urban environment, a signal reliability map is introduced, which provides information about regions where large errors due to cellular signal multipath or poor GNSS line-of-sight (LOS) are expected. The vehicle uses the signal reliability map to calculate the position estimation mean-squared error (MSE). An analytical expression for the AGV's state estimates is derived for a weighted nonlinear least-squares (WNLS) estimator, which is used to find an analytical upper bound on the position bias due to multipath. A path planning approach

based on Dijkstra's algorithm is proposed to optimize the AGV's path while minimizing the path length and the position estimation MSE, subject to keeping the position estimation uncertainty and position estimation bias due to multipath being below desired thresholds. The path planning approach yields the optimal path together with a list of feasible paths. Simulation results are presented demonstrating that utilizing ambient cellular LTE signals together with GNSS signals (1) reduces the uncertainty about the AGV's position, (2) increases the number of feasible paths to choose from, which could be useful if other considerations arise, e.g., traffic jams and road blockages due to construction, and (3) yields significantly shorter feasible paths, which would otherwise be infeasible with GNSS signals alone. Experimental results on a ground vehicle navigating in downtown Riverside, California, are presented demonstrating a close match between the simulated and experimental results.

Contents

List of Figures

List of Tables

Chapter 1

Introduction

Autonomous ground vehicles (AGVs) are said to improve quality of life by reducing human error and automating monotonous tasks. The field is also an area of economic gain, as shown by several large corporations investing in research for AGVs for applications including cargo delivery, taxi services, and transportation [1]. However, in light of recent tragedies [10], autonomous vehicles are not yet fully accepted by the public, and it is evident that reliable navigation systems are necessary. Most navigation systems use Global Navigation Satellite System (GNSS) technology, which has been the heart of navigation over the last few decades, but can be challenged in urban environments. Urban high-rise structures block, shadow, and reflect signals from satellites, thereby limiting the accuracy of the calculated position. This shows a relationship between the location of the GNSS receiver and the accuracy in the position estimate. To this end, path planning while optimizing over position accuracy (i.e., biases and uncertainty) can be used to improve AGV navigation.

The goal of path planning, also known as motion planning or trajectory generation,

is to optimize a path over a defined objective (e.g., path length, path duration, position uncertainty). In robotics, path planning is used to localize the robot while generating a map of the environment. For an autonomous robot which uses simultaneous localization and mapping (SLAM), a method for path planning while minimizing over the probability of becoming lost is considered in [62], where *a priori* information about textured areas in the environment is used. A path planner that optimizes for viewpoint coverage to reconstruct an unknown environment without *a priori* knowledge is proposed in [40]. Vehicle dynamics, position uncertainty, and obstacle volume are accounted for in [42], where the Lagrange-Euler equations and a potential field-based method are used for predictive and multirate reactive planning for intelligent vehicles. In other contexts, target tracking uses path planning to estimate the position of a separate moving object. In [60], a motion tracking problem is proposed that minimizes the time between observations of a target made by several mobile unmanned aerial vehicle's (UAVs). A cooperative urban environment target tracking algorithm that uses UAVs and AGVs and accounts for obstacles is proposed in [66], where the objective is to maximize the time that a target is observed. Motion planning in spatiotemporal signal landscape maps to maximize the information gathered from ambient signals to yield accurate positioning was considered in [25, 27, 28, 30].

In this work, path planning is used to find a path for an AGV such that the vehicle can navigate reliably. Current research examines path planning to optimize over AGV location uncertainty. A partially observable Markov decision process (POMDP) is used in [20] for belief state planning, which accounts for uncertainty from noise in sensor data and the intentions of human drivers. Research in path planning also accounts for vehicles

that use GNSS signals. In [46], a path planning framework is proposed that accounts for uncertainty in position estimation from GNSS satellites by using dilution of precision (DOP). Current research also demonstrates using both position uncertainty and multipath in GNSS signals for planning routes for ground vehicles. A method for optimal routing was proposed in [24] to predict GNSS quality of service (QoS) along a route using QoS parameters, i.e., availability, accuracy, reliability, and continuity.

Although GNSS navigation is prevalent, it can be challenged in urban environments due to high-rise structures, which block, shadow, and reflect signals causing measurement errors. Therefore, unlike previous work, this thesis exploits ambient cellular signals of opportunity (SOPs) (SOPs include digital television (DTV), Wi-Fi, satellite communications, and cellular 2G/3G/4G signals [36,39,44,47]) to improve availability. Cellular signals are particularly attractive SOPs due to their geometric diversity and high received signal power [31, 47]. To this end, the AGV considered in this thesis navigates with GNSS and cellular measurements, and a new path planning generator prescribes a short path from a start to a target point which uses reliable GNSS and cellular measurements which ensures the positioning errors are minimal. The path planning generator accounts for position errors by calculating cellular pseudorange measurement biases and GNSS line of sight (LOS) through familiar and meaningful metrics, such as position estimation mean-squared-error (MSE).

Some key assumptions are made in this thesis. One assumption is that multipath does not need to be accounted for in GNSS signals, but it does need to be accounted for in cellular signals. Cellular signals suffer from severe multipath errors primarily due to

low elevation angles in urban environments [54]. Although there is current research in multipath mitigation for cellular pseudoranges, multipath is still the dominating source of measurement bias [13, 19, 53, 55–58]. In contrast, commercial GNSS receivers use multipath mitigation techniques [16]. Therefore, multipath biases in only cellular signals is accounted for in path planning. The second assumption is that the cost function (a function of GNSS satellite geometry) from the departure time through the time the AGV arrives at the target position is the same. This assumption is made for simplicity, and is reasonable for AGV paths with short duration since the satellite geometry changes slowly. This assumption is further justified later.

The contributions of this thesis are fourfold. First, the thesis introduces GNSS and cellular signal reliability maps, which stores information about areas where GNSS satellites have unobstructed LOS, and areas where cellular pseudorange measurements produce large errors due to multipath. Second, the thesis proposes a method for calculating the position estimation MSE to indicate the expected quality of the position estimation at each specified location and time along the road network. Third, an analytical expression for the position bias is obtained to find an upper bound on the position bias due to multipath, which is shown to be parameterized by a bound on the pseudorange bias and the uncertainty measure (i.e., the largest eigenvalue of the position error covariance). Fourth, the thesis proposes a method for path planning using path length, position MSE, and the largest eigenvalue of the position error covariance.

The contributions are demonstrated and validated in computer simulations and experimental scenarios with real data. It was shown that including a cellular LTE receiver

4

can increase the number of feasible paths, and "open up" areas that are infeasible with GNSS only. Experimental results show an improvement in the position root-mean-squared error (RMSE) when choosing the prescribed path instead of an alternate path, and that the simulated results were consistent with the experimental results when the environment is known accurately. Also, results were shown for an AGV that does not use the proposed algorithm and instead takes the shortest path, and demonstrates the importance of planning the path of an AGV to avoid situations where the AGV could not estimate its state.

This thesis is organized as follows. Chapter II formulates the problem, and Chapter III describes the navigation frameworks used in this thesis. Chapter IV presents the method for calculating GNSS and cellular signal reliability maps, which refers to the map of areas where the radio navigation signals are expected to produce large pseudorange errors due to multipath or limited LOS to the transmitters. Chapter V shows how to calculate the position estimation MSE using the signal reliability maps, and finds an upper bound on the position bias. Chapter VI describes the method for path planning, which uses path length, position estimation MSE, and parameters of the upper bound on the position bias. Finally, Chapter VII shows the simulation results, and Chapter VIII shows the experimental results.

Chapter 2

Problem Description

This thesis considers the following problem. An AGV drives in an urban environment. The vehicle is equipped with receivers capable of producing pseudorange measurements on GNSS satellites and nearby cellular towers. The AGV uses these pseudorange measurements to estimate its state. The AGV desires to reach a target location by taking the shortest possible path, while guaranteeing that the uncertainty about it's own position estimate is below a specified threshold (e.g., for safety concerns). A trajectory that satisfies this objective is generated either locally (i.e., within the AGVs processor) or at a cloud-hosted path planning generator. The path planning generator uses a geographic information system (GIS) three-dimensional (3-D) building map of the environment to generate a so-called signal reliability map. The signal reliability map is a spatiotemporal map of the environment that measures the expected accuracy from using GNSS and cellular signals to produce an estimate of the AGVs state. For GNSS signals, the signal reliability map specifies to which GNSS satellites the AGV would have a clear LOS for different loca-

tions at different times in the environment. For cellular signals, the signal reliability map specifies the expected pseudorange bias due to multipath. The signal reliability maps are used to calculate the position MSE at each location, which in turn is used to generate an optimal path for the AGV to follow. This path is generated by minimizing the distance and MSE, while guaranteeing that the bias in the position estimate due to multipath is below a desired threshold as well as ensuring that the maximum position uncertainty is below a desired limit. In addition, the path generator produces a table of reliable GNSS satellites and cellular towers for the AGV to use as it executes the optimal path. Fig. 2.1 illustrates a flowchart of the optimal path generator framework developed in this thesis.
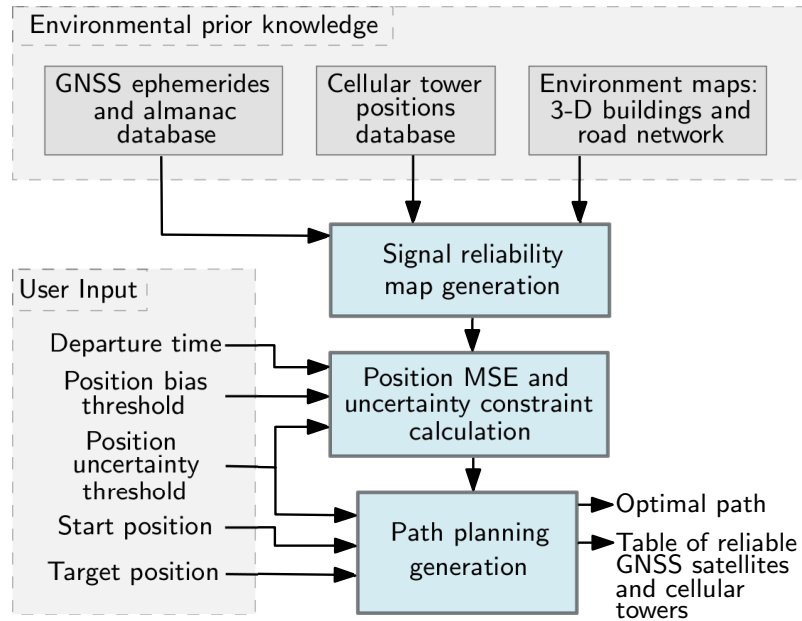
Figure 2.1: Flowchart of the proposed path planning generator. The path planning generator is assumed to have knowledge of GNSS orbital data, cellular tower positions, and 3-D environment map. The user inputs are: departure time, start position, target position, position bias threshold, and position uncertainty threshold. The thresholds are used as constraints to find the optimal path. The outputs of the path planning generator are the optimal path and a table of reliable GNSS satellites and cellular towers to use along the optimal path.

Fig. 2.2 depicts the objective of the optimal path planning generator. Here, the red circles on the street represent locations that violate the user-specified constraints (position bias or position uncertainty exceeding their respective thresholds).
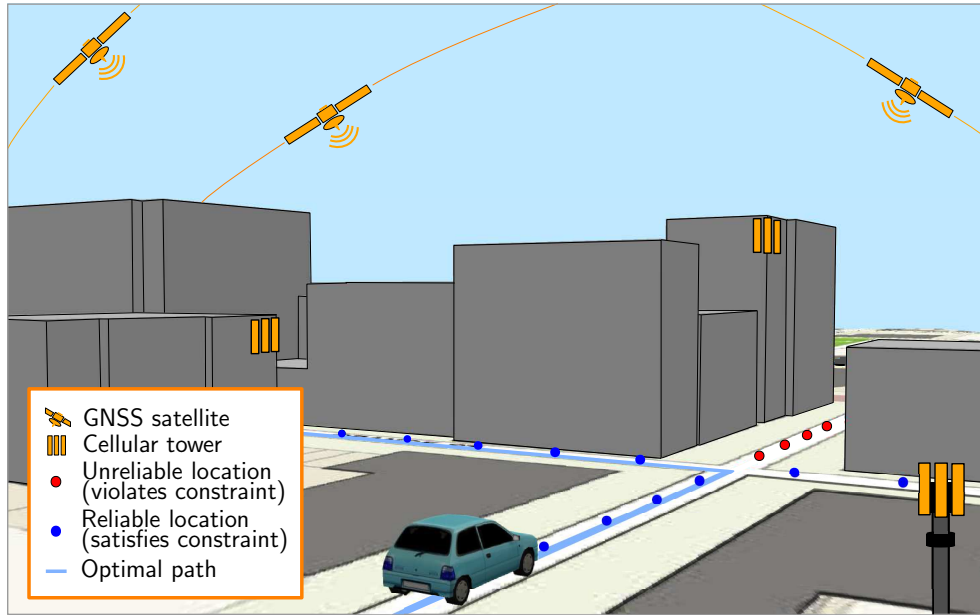
Figure 2.2: Depiction of an AGV navigating with GNSS and cellular signals. Here, the red circles represent locations where GNSS and cellular signals are unreliable (i.e., the position estimate produced with such signals will violate position bias and uncertainty constraints) due to limited LOS to GNSS satellites and/or large cellular multipath errors. The blue circles represent locations where GNSS and cellular signals are reliable. The proposed framework generates the optimal blue trajectory, which satisfies the constraints, while minimizing the distance traveled between the start and target positions together with minimizing the position MSE. This figure is obtained with ArcGIS® [3].

The following chapter describes the AGV-mounted receiver states, measurements, and estimation algorithm.

Chapter 3

Model Description and Estimation

Algorithm

3.1 AGV-Mounted Receiver States

The AGV receives signals from M spatially-stationary cellular towers. It is assumed that the coordinates of the cellular towers are known *a priori* (e.g., via radio mapping or satellite images [26, 43]) and are stored locally or on a cloud-hosted database. The 3-D position of the m-th cellular tower is denoted $\boldsymbol{r}_{\mathrm{SOP},m} \triangleq [x_{\mathrm{SOP},m}, y_{\mathrm{SOP},m}, z_{\mathrm{SOP},m}]^{\mathsf{T}}$. The AGV also receives signals from N GNSS satellites with known positions. The 3-D position of the n-th GNSS satellite is denoted $\boldsymbol{r}_{\mathrm{SV},n} \triangleq [x_{\mathrm{SV},n}, y_{\mathrm{SV},n}, z_{\mathrm{SV},n}]^{\mathsf{T}}$.

The unknown states include the vehicle's 3-D position $\boldsymbol{r}_r \triangleq [x_r, y_r, z_r]^{\mathsf{T}}$, the AGV-mounted receiver's clock bias δt_r, and the clock bias of the M cellular towers $\{\delta t_{\mathrm{SOP},m}\}_{m=1}^{M}$. The cellular LTE technical specification requires transmitters in neighboring cells to be

synchronized in phase up to 10 μs [11]. Many cellular providers synchronize nearby towers in a much tighter fashion as was demonstrated in recent experimental studies [34,35]. This synchronization will be exploited in the proposed estimation framework to minimize the number of states that will be estimated. Specifically, only the clock bias of one of the towers will be estimated (referred to as the first tower, without loss of generality). The clock bias of the other cellular towers will be expressed as deviations from the clock bias of the first tower. The model of such deviation and the estimation algorithm will be discussed in the following subsections.

3.2 AGV Measurements

The AGV-mounted receiver makes pseudorange measurements to the N GNSS satellites. The n-th GNSS pseudorange measurement is modeled as

$$\rho_{\mathrm{SV},n}(k) = \|\boldsymbol{r}_r(k) - \boldsymbol{r}_{\mathrm{SV},n}\|_2 + c[\delta t_r(k) - \delta t_{\mathrm{SV},n}(k)]$$

$$+ c\delta t_{\mathrm{iono},n}(k) + c\delta t_{\mathrm{tropo},n}(k) + v_{\mathrm{SV},n}(k),$$

where c is the speed of light, $\delta t_{\mathrm{iono},n}$ and $\delta t_{\mathrm{tropo},n}$ are known ionospheric and tropospheric delays, respectively, and $\delta t_{\mathrm{SV},n}$ is the known satellite clock bias. The terms $\boldsymbol{r}_{\mathrm{SV},n}$, $\delta t_{\mathrm{iono},n}$, $\delta t_{\mathrm{tropo},n}$, and $\delta t_{\mathrm{SV},n}$ are given in the satellite's navigation message. The term $v_{\mathrm{SV},n}$ is the measurement noise, which is modeled as a zero-mean white Gaussian random sequence with variance $\sigma^2_{\mathrm{SV},n}$. The measurements noise across different satellites $\{v_{\mathrm{SV},n}\}_{n=1}^N$ are assumed to be independent. The n-th GNSS pseudorange measurement is modified by subtracting

the known $\delta t_{\mathrm{iono},n}$, $\delta t_{\mathrm{tropo},n}$, and $c\delta t_{\mathrm{SV},n}$ to yield

$$z_{\mathrm{SV},n} \triangleq \rho_{\mathrm{SV},n} - c\delta t_{\mathrm{iono},n} - c\delta t_{\mathrm{tropo},n} + c\delta t_{\mathrm{SV},n}$$

$$= \|\boldsymbol{r}_r - \boldsymbol{r}_{\mathrm{SV},n}\|_2 + c\delta t_r + v_{\mathrm{SV},n}. \tag{3.1}$$

The AGV-mounted receiver also makes pseudorange measurements to the M cellular towers. The m-th cellular pseudorange measurement is modeled as [29]

$$\rho_{\mathrm{SOP},m}(k) = \|\boldsymbol{r}_r(k) - \boldsymbol{r}_{\mathrm{SOP},m}\|_2 + c[\delta t_r(k) - \delta t_{\mathrm{SOP},m}(k)] + v_{\mathrm{SOP},m}(k),$$

where $v_{\mathrm{SOP},m}$ is the measurement noise, which is modeled as a zero-mean white Gaussian sequence with variance $\sigma_{\mathrm{SOP},m}^2$. The measurement noise across different cellular towers $\{v_{\mathrm{SOP},m}\}_{m=1}^{M}$ are assumed to be independent. By exploiting the synchronization between nearby cellular towers, the transmitter clock bias of the m-th cellular measurement can be expressed as

$$c\delta t_{\mathrm{SOP},m}(k) = c\delta t_{\mathrm{SOP},1}(k) + \epsilon_m + v_{\epsilon,m}(k), \tag{3.2}$$

for $m = 2, \ldots, M$, where ϵ_m is a deterministic constant bias and $v_{\epsilon,m}$ is approximated as a zero-mean white noise sequence with variance $\sigma_{\epsilon,m}^2$. Therefore, for all cellular measurements other than the first cellular measurement, the m-th cellular pseudorange can be rewritten in terms of $c\delta t_{\mathrm{SOP},1}$, i.e.,

$$\rho_{\mathrm{SOP},m}(k) = \|\boldsymbol{r}_r(k) - \boldsymbol{r}_{\mathrm{SOP},m}\|_2 + c\delta t_r(k) - c\delta t_{\mathrm{SOP},1}(k) - \epsilon_m + v'_{\mathrm{SOP},m}(k), \tag{3.3}$$

for $m = 2, \ldots, M$, where $v'_{\mathrm{SOP},m} \triangleq v_{\mathrm{SOP},m} - v_{\epsilon,m}$ is a zero-mean white noise sequence with variance $\sigma_{\mathrm{SOP},m}^2 + \sigma_{\epsilon,m}^2$.

Using (3.2), the cellular pseudorange measurement (3.3) to the M cellular towers is modified according to

$$z_{\text{SOP},1}(k) = \|\boldsymbol{r}_r(k) - \boldsymbol{r}_{\text{SOP},1}\|_2 + c\left[\delta t_r(k) - \delta t_{\text{SOP},1}(k)\right] + v_{\text{SOP},1}(k),$$

$$z_{\text{SOP},m}(k) \triangleq \rho_{\text{SOP},m}(k) + \epsilon_m$$

$$= \|\boldsymbol{r}_r(k) - \boldsymbol{r}_{\text{SOP},m}\|_2 + c\left[\delta t_r(k) - \delta t_{\text{SOP},1}(k)\right] + v'_{\text{SOP},m}(k),$$

for $m = 2, \ldots, M$. The next subsection describes an estimation procedure for ϵ_m and $\sigma^2_{\epsilon,m}$.

3.3 Estimation of Cellular Measurement Clock Bias Perturbations

The perturbation parameters of the m-th cellular clock bias from the first cellular clock bias (eq. (3.2)), namely, the constant bias ϵ_m and the variance $\sigma^2_{\epsilon,m}$ can be estimated by the AGV locally or assumed to be available from a cloud-hosted database. To estimate the constant bias ϵ_m and variance $\sigma^2_{\epsilon,m}$, the measurements are differenced according to

$$\rho_{\text{SOP},1}(k) - \rho_{\text{SOP},m}(k) = \|\boldsymbol{r}_r(k) - \boldsymbol{r}_{\text{SOP},1}\|_2 - \|\boldsymbol{r}_r(k) - \boldsymbol{r}_{\text{SOP},m}\|_2 \qquad (3.4)$$

$$+ \epsilon_m + v_{\text{SOP},1}(k) - v'_{\text{SOP},m}(k).$$

It is assumed that the differencing operation in (3.4) is performed in an open area where $\boldsymbol{r}_r$ is accurately estimated (e.g., while the AGV is initially stationary with clear LOS to GNSS satellites). Subsequently, define the measurement

$$z_{\text{init},m}(k) = \rho_{\text{SOP},1}(k) - \rho_{\text{SOP},m}(k) - \|\boldsymbol{r}_r(k) - \boldsymbol{r}_{\text{SOP},1}\|_2 + \|\boldsymbol{r}_r(k) - \boldsymbol{r}_{\text{SOP},m}\|_2$$

$$= \epsilon_m + v_{\text{SOP},1}(k) - v_{\text{SOP},m}(k) + v_{\epsilon,m}(k).$$

Assuming the measurement noise to be ergodic, ϵ_m and $\sigma^2_{\epsilon,m}$ can be estimated using a sample mean and a sample variance over K measurements, namely

$$\hat{\epsilon}_m = \frac{1}{K} \sum_{k=1}^{K} z_{\text{init},m}(k)$$

$$\widehat{\sigma^2_{\epsilon,m}} = \left[\frac{1}{K-1} \sum_{k=1}^{K} [z_{\text{init},m}(k) - \hat{\epsilon}_m]^2 \right] - \sigma^2_{\text{SOP},1} - \sigma^2_{\text{SOP},m}.$$

The value of K can be a fixed value chosen prior to the initialization, or can be determined during initialization by increasing K until the sample mean and variance converge. Experimentally, it was observed that the sample mean and variance converged in around 0.5 seconds with measurements at a sampling time $T = 0.1$ seconds (i.e., $K \approx 50$ samples).

3.4   AGV State Estimation

The AGVs state vector defined as $\boldsymbol{x}_r \triangleq \left[\boldsymbol{r}_r^\mathsf{T}, c\delta t_r, c\delta t_{\text{SOP},1} \right]^\mathsf{T}$ is estimated from the measurement vector $\boldsymbol{z}_r \triangleq [z_{\text{SV},1}, \ldots, z_{\text{SV},N}, z_{\text{SOP},1}, \ldots, z_{\text{SOP},M}]^\mathsf{T}$ through a weighted non-linear least squares (WNLS) estimator.

The measurement Jacobian used in the WNLS estimator is $\mathbf{H} \triangleq [\mathbf{G}, \mathbf{B}]$, where

$$\mathbf{G} \triangleq \left[\mathbf{G}_{\text{SV}}^\mathsf{T}, \mathbf{G}_{\text{SOP}}^\mathsf{T} \right]^\mathsf{T},$$

$$\mathbf{G}_{\text{SV}} \triangleq \begin{bmatrix} \frac{\boldsymbol{r}_r^\mathsf{T} - \boldsymbol{r}_{\text{SV},1}^\mathsf{T}}{\left\| \boldsymbol{r}_r - \boldsymbol{r}_{\text{SV},1} \right\|_2} \\ \vdots \\ \frac{\boldsymbol{r}_r^\mathsf{T} - \boldsymbol{r}_{\text{SV},N}^\mathsf{T}}{\left\| \boldsymbol{r}_r - \boldsymbol{r}_{\text{SV},N} \right\|_2} \end{bmatrix}, \quad \mathbf{G}_{\text{SOP}} \triangleq \begin{bmatrix} \frac{\boldsymbol{r}_r^\mathsf{T} - \boldsymbol{r}_{\text{SOP},1}^\mathsf{T}}{\left\| \boldsymbol{r}_r - \boldsymbol{r}_{\text{SOP},1} \right\|_2} \\ \vdots \\ \frac{\boldsymbol{r}_r^\mathsf{T} - \boldsymbol{r}_{\text{SOP},M}^\mathsf{T}}{\left\| \boldsymbol{r}_r - \boldsymbol{r}_{\text{SOP},M} \right\|_2} \end{bmatrix},$$

and

$$\mathbf{B} \triangleq \begin{bmatrix} \mathbf{1}_{N \times 1} & \mathbf{0}_{N \times 1} \\ \mathbf{1}_{M \times 1} & -\mathbf{1}_{M \times 1} \end{bmatrix}, \tag{3.5}$$

13

where $\mathbf{1}$ and $\mathbf{0}$ are matrices of ones and zeros respectively.

The weighting matrix in the WNLS is chosen as inverse of the measurement noise covariance $\mathbf{R} = \text{diag}[\sigma_{\text{SV},1}^2, \ldots, \sigma_{\text{SV},N}^2, \sigma_{\text{SOP},1}^2, \sigma_{\text{SOP},2}^2 + \sigma_{\epsilon,2}^2, \ldots, \sigma_{\text{SOP},M}^2 + \sigma_{\epsilon,M}^2]$.

Chapter 4

Signal Reliability Map Generation

A signal reliability map is a spatiotemporal map specifying for each location in the road network: (i) the GNSS satellite to which there is a clear LOS and (ii) the pseudorange multipath error produced for each cellular tower. The following sections define the signal reliability maps for GNSS and cellular signals and discuss how they can be generated and stored.

4.1 GNSS Signal Reliability Map Generation

GNSS signals suffer from multipath interference and non-line of sight (NLOS) conditions in urban environments. Multipath interference in urban environments is a dominant error source to which many mitigation techniques have been proposed [16, 33, 38, 69]. Receiver-based multipath mitigation techniques typically require the LOS signal to be received [22, 64], while more advanced techniques in NLOS conditions require specialized antennas and additional hardware [18, 21, 49].

15

The proposed approach in this thesis will only consider GNSS satellites to which there is a clear LOS. To this end, the signal reliability map for GNSS signals stores information about whether the LOS path between the receiver and satellite is obstructed. Since GNSS satellite positions change with time, the GNSS signal reliability maps store the time intervals when a satellite is visible at a given location. The intervals are stored for each satellite and each location.

Formally, the GNSS signal reliability map for a given satellite is a sequence with P elements, where each element represents a location in the road network. The environment consists of N transmitters. The signal reliability map for the n-th satellite is

$$\mathcal{M}_{\mathrm{SV}_n} = \{\mathcal{T}_{\mathrm{SV}_n,p}\}_{p=1}^{P}, \quad \text{for } n = 1, \ldots, N.$$

Here, p represents a unique index corresponding to a particular location in the road network. Each $\mathcal{T}_{\mathrm{SV}_n,p}$ is a sequence of ordered pairs representing the start and end times for which the n-th satellite has unobstructed LOS at location p, i.e.,

$$\mathcal{T}_{\mathrm{SV}_n,p} = \left\{(t_{\mathrm{start},p,\tau}, t_{\mathrm{end},p,\tau})\right\}_{\tau=1}^{T_\tau}.$$

For one day, there are a total of T_τ time intervals with start and end times $t_{\mathrm{start},p,\tau}$ and $t_{\mathrm{end},p,\tau}$, respectively. Since the satellite ephemeris data is known and due to the periodicity of GNSS satellites [51, 52], the GNSS signal reliability map could be generated *a priori* and updated infrequently, whenever the environment undergoes certain changes (e.g., construction of a new building or demolition of an old one). The signal reliability map can be stored locally at the vehicle or at a cloud-hosted database. At a location p, the n-th satellite has unobstructed LOS at time t if

$$t_{\mathrm{start},p,\tau} \leq t \leq t_{\mathrm{end},p,\tau}, \quad \text{for any } \tau = 1, \ldots, T_\tau.$$

The signal reliability maps for N satellites are collectively referred to by $\mathcal{M}_{\mathrm{SV}} = \{\mathcal{M}_{\mathrm{SV}_n}\}_{n=1}^{N}$.
Fig. 4.1 shows a visualization of GNSS signal reliability maps. Here, Fig 4.1 (a) shows a region in downtown Riverside, California in which signal blockage for a particular GNSS satellite is depicted as a two-dimensional (2-D) red polygon. Fig. 4.1 (b) overlays the maps of 12 different GNSS satellites to yield a heat-type map representing the number of satellites to which there is NLOS.
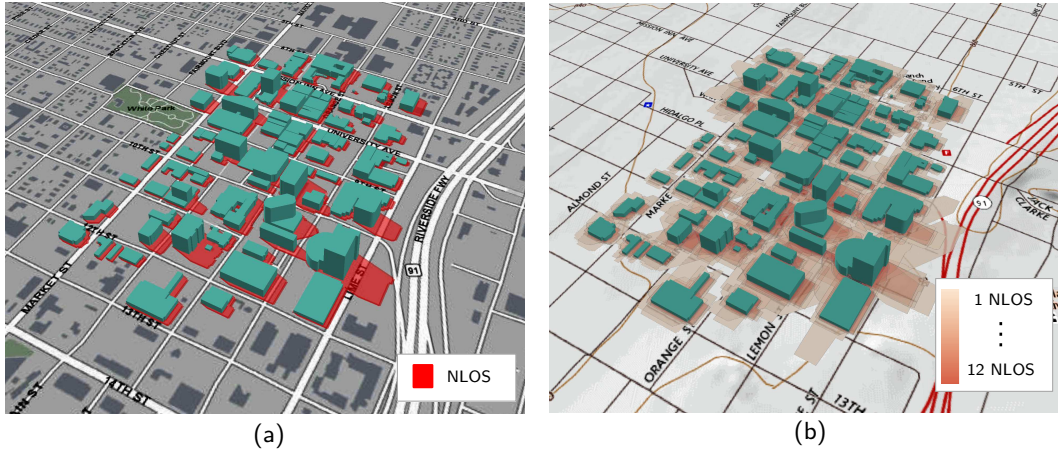
Figure 4.1: Visualization of GNSS signal reliability maps. (a) A region in downtown Riverside, California in which signal blockage to a particular GNSS satellite is depicted as a 2-D red polygon. (b) The polygon layers corresponding to 12 different satellites overlayed to generate a heat-type map representing the number of satellites to which there is NLOS. This figure is obtained with ArcGIS® [3].

For a given time, signal reliability maps are visualized as point features, but they can also be visualized as a polygon layer or raster feature. This work can be extended to account for GNSS multipath bias, utilizing previously developed algorithms for simulating multipath bias for GNSS signals [33, 37, 50].

4.2 Cellular Signal Reliability Map Generation

In contrast to GNSS signals, cellular signals are often received at low elevation angles, which makes them more susceptible to multipath-induced errors. While multipath mitigation techniques for cellular signals has been an active area of research recently, multipath continues to be among the most dominating sources or error, thereby inducing a large pseudorange measurement bias. This is particularly the case whenever the reflected signal has a higher power than the LOS signal [13, 19, 56].

The cellular signal reliability map stores simulated pseudorange bias caused by multipath. The bias is found using the complex channel impulse response, which provides information about arrival time, phase, and power of each signal path. The complex channel impulse response can be readily calculated using proprietary simulation software (e.g., Wireless Insite [9]). This calculation requires knowledge about the cellular environment, including transmitter location, signal characteristics, antenna type, 3-D building map of the environment, and receiver location. This is carried out for all M cellular transmitters and different receiver locations within the environment. In what follows, the multipath bias calculation from the channel impulse response is discussed.

At each receiver location, the impulse response for the i-th LTE orthogonal frequency-division multiplexing (OFDM) symbol is given by

$$h_i(t) = \sum_{x=0}^{x=X-1} a_i(x)\delta(\tau - \tau_i(x)), \qquad (4.1)$$

where X is the number of impulses, $a_i(x)$ corresponds to the complex-valued amplitude, and $\tau_i(x)$ is the corresponding path delay. The complex channel impulse response (4.1) can be used to measure the multipath interference, $\chi_m \triangleq \chi_{1,m}(i) + \chi_{2,m}(i)$, for $m = 1, \ldots, M$,

where,

$$\chi_{1,m}(i) = A \left| \sum_{l=0}^{L-1} \sum_{x=1}^{X-1} a_i(x) e^{-j2\pi(l/L)(\tau_i(x)/T_s + \tilde{e}_\theta - \xi)} \right|^2 \tag{4.2}$$

$$- A \left| \sum_{l=0}^{L-1} \sum_{x=1}^{X-1} a_i(x) e^{-j2\pi(l/L)((\tau_i(x)/T_s) + \tilde{e}_\theta + \xi)} \right|^2,$$

$$\chi_{2,m}(i) = 2A\Re\left[\left(\sum_{l=0}^{L-1} e^{-j2\pi(l/L)(\tilde{e}_\theta - \xi)} \right) \cdot \left(\sum_{l'=0}^{L-1} \sum_{x=1}^{X-1} a_i^*(x) e^{j2\pi(l'/L)(\tau_i(x)/T_s + \tilde{e}_\theta - \xi)} \right) \right] \tag{4.3}$$

$$- 2A\Re\left[\left(\sum_{l=0}^{L-1} e^{-j2\pi(l/L)(\tilde{e}_\theta + \xi)} \right) \cdot \left(\sum_{l'=0}^{L-1} \sum_{x=1}^{X-1} a_i^*(x) e^{j2\pi(l'/L)(\tau_i(x)/T_s + \tilde{e}_\theta + \xi)} \right) \right],$$

where $\Re[\cdot]$ denotes the real part, T_s is the sampling interval, $0 < \xi \leq 0.5$ is the time shift

in the LTE receiver's tracking loop ($\xi = 0.5$ is chosen in this thesis), L is the number of

subcarrier symbols in the pilot (200 when the bandwidth is 20 MHz and the cell-specific

reference signal (CRS) is used as the pilot), and A is the signal power due to antenna gain

and implementation loss [53, 65]. The normalized symbol timing error $\tilde{e}_\theta$ is set to zero to

assume perfect tracking. Using (4.2) and (4.3), the multipath interference χ_m for all M

cellular transmitters is determined.

The multipath bias is comprised of the multipath interference χ_m and the NLOS

bias (i.e., path delay between the first received path and the LOS path). That is, the

multipath bias is given by

$$b_{m,p} \triangleq \chi_m + c\tau_i(0) - d_{\text{LOS}}, \tag{4.4}$$

where d_{LOS} is the length of the LOS path. If $|a_i(x)| < \kappa$, for all $x = 0, \ldots, X-1$, where κ

is a threshold, the LTE signal is rendered too weak to be tracked and the signal reliability

map assumes no cellular measurement at that location. For each cellular transmitter, the

bias is stored for each location in the cellular signal reliability map. Formally, the cellular signal reliability map for the m-th transmitter is a sequence with P elements

$$\mathcal{M}_{\mathrm{SOP}_m} = \{b_{m,p}\}_{p=1}^{P},$$

where $b_{m,p} = \varnothing$ when the m-th cellular measurement is not received at the p-th location, where $\varnothing$ denotes null. The signal reliability maps for M LTE transmitters are collectively referred to by $\mathcal{M}_{\mathrm{SOP}} = \{\mathcal{M}_{\mathrm{SOP}_m}\}_{m=1}^{M}$.

Fig. 4.2 shows a visualization of a cellular signal reliability map for a single cellular tower corresponding to the U.S. cellular provider AT&T in downtown Riverside, California. A raster feature is illustrated, where the black regions indicate that (i) the pseudorange bias due to multipath at the p-th location exceeds a threshold $\eta_{\max} = 0.5$ m, i.e., $b_{m,p} \geq 0.5$ or (ii) there is no cellular measurement, i.e., $b_{m,p} = \varnothing$ at the p-th position. The threshold $\eta_{\max}$ is the pseudorange bias threshold used in the path planning optimization problem explained in Section 5.2 and Chapter 6.
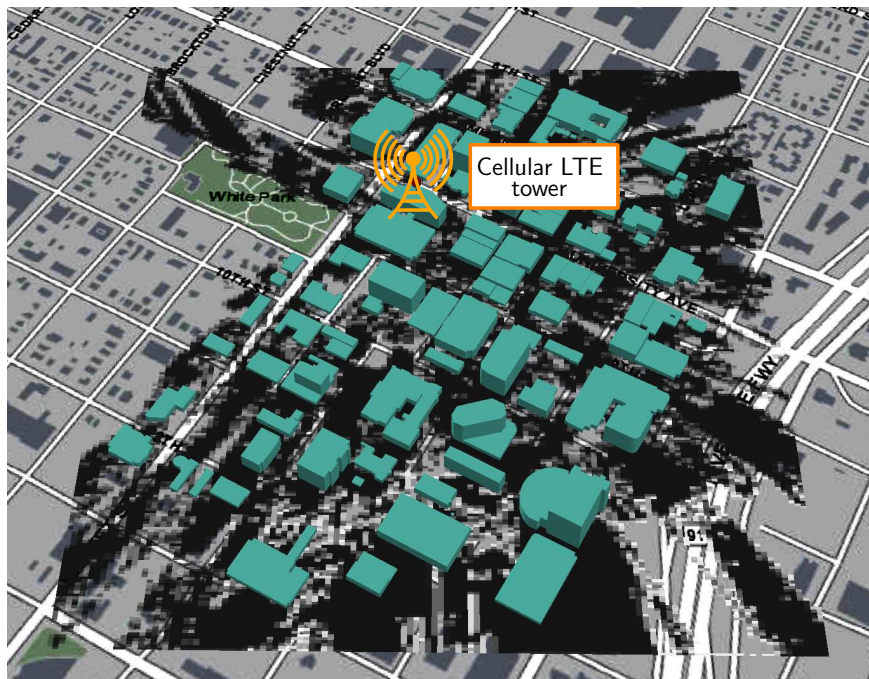
Figure 4.2: A visualization of the cellular signal reliability map. The black regions indicate that (i) the pseudorange bias due to multipath at the p-th location exceeds a threshold $\eta_{\max} = 0.5$ m, i.e., $b_{m,p} \geq 0.5$ or (ii) there is no cellular measurement, i.e., $b_{m,p} = \varnothing$ at the p-th position. This figure is obtained with ArcGIS® [3].

Chapter 5

Position MSE and Uncertainty

Constraint Calculation

This chapter describes the formulation of the optimization function and constraints used to generate the optimal path. The optimization function involves the position MSE, which is discussed in the first section, while the constraint involves the largest eigenvalue of the position estimation error covariance, which is discussed in the second section.

In what follows, the biased and unbiased error states are formally defined based on the measurement model and the estimator. Since the measurement model is nonlinear with respect to the state vector $\boldsymbol{x}_r$, the model is linearized according to

$$\boldsymbol{\Delta z_r} = \mathbf{H}\boldsymbol{\Delta x}_r + \boldsymbol{v},$$

where the $\boldsymbol{\Delta z_r}$ is the measurement error vector, which is the difference between the measurement vector $\boldsymbol{z}_r$ and its estimate $\hat{\boldsymbol{z}}_r$; $\boldsymbol{\Delta x}_r \triangleq \boldsymbol{x}_r - \hat{\boldsymbol{x}}_r$, i.e., $\boldsymbol{\Delta x}_r$ is the estimation error, which is the difference between $\boldsymbol{x}_r$ and the WNLS estimate $\hat{\boldsymbol{x}}_r$, and $\boldsymbol{v} \triangleq$

$[v_{\mathrm{SV},1}, \ldots, v_{\mathrm{SV},N}, v_{\mathrm{SOP},1}, \ldots, v_{\mathrm{SOP},M}]^{\mathsf{T}}$. To analyse the effect of multipath bias, a deterministic bias $\boldsymbol{b}$ is introduced in the measurement,

$$\boldsymbol{\Delta z_r} \triangleq \boldsymbol{\Delta z_r}' + \boldsymbol{b},$$

where $\boldsymbol{\Delta z_r'} = [\boldsymbol{\Delta z_{r\mathrm{SV}}'}^{\mathsf{T}}, \boldsymbol{\Delta z_{r\mathrm{SOP}}'}^{\mathsf{T}}]^{\mathsf{T}}$ is the unbiased measurement error vector.

The effect of the pseudorange bias on the position estimate can be found through the normal equation (see, for example, eqn. (7.67) in [23])

$$\boldsymbol{\Delta x_r} = (\mathbf{H}^{\mathsf{T}}\mathbf{R}^{-1}\mathbf{H})^{-1}\mathbf{H}^{\mathsf{T}}\mathbf{R}^{-1}\boldsymbol{\Delta z_r}$$

$$= (\mathbf{H}^{\mathsf{T}}\mathbf{R}^{-1}\mathbf{H})^{-1}\mathbf{H}^{\mathsf{T}}\mathbf{R}^{-1}(\boldsymbol{\Delta z_r'} + \boldsymbol{b})$$

$$= (\mathbf{H}^{\mathsf{T}}\mathbf{R}^{-1}\mathbf{H})^{-1}\mathbf{H}^{\mathsf{T}}\mathbf{R}^{-1}\boldsymbol{\Delta z_r'} + (\mathbf{H}^{\mathsf{T}}\mathbf{R}^{-1}\mathbf{H})^{-1}\mathbf{H}^{\mathsf{T}}\mathbf{R}^{-1}\boldsymbol{b}.$$

Therefore, the bias in the pseudorange introduces an additive bias in the estimation error according to

$$\boldsymbol{\Delta x_r} = \boldsymbol{\Delta x_r'} + \boldsymbol{x}_{r,\mathrm{err}},$$

where $\boldsymbol{x}_{r,\mathrm{err}} \triangleq [\boldsymbol{r}_{r,\mathrm{err}}^{\mathsf{T}}, c\boldsymbol{\delta t}_{\mathrm{err}}^{\mathsf{T}}]^{\mathsf{T}}$ results from the multipath bias in the measurement, and $\boldsymbol{\Delta x_r'} \triangleq [\boldsymbol{\Delta r_r'}^{\mathsf{T}}, c\boldsymbol{\Delta \delta t'}^{\mathsf{T}}]^{\mathsf{T}}$ is the unbiased state estimation error. The vector $\boldsymbol{\delta t}$ represents the vector of clock bias states. Therefore, the unbiased state estimation error and the state bias can be respectively expressed as

$$\boldsymbol{\Delta x_r'} = (\mathbf{H}^{\mathsf{T}}\mathbf{R}^{-1}\mathbf{H})^{-1}\mathbf{H}^{\mathsf{T}}\mathbf{R}^{-1}\boldsymbol{\Delta z_r'},$$

$$\boldsymbol{x}_{r,\mathrm{err}} = (\mathbf{H}^{\mathsf{T}}\mathbf{R}^{-1}\mathbf{H})^{-1}\mathbf{H}^{\mathsf{T}}\mathbf{R}^{-1}\boldsymbol{b}. \tag{5.1}$$

The following section explains the steps for using the GNSS and cellular signal reliability maps whose generation was described in Chapter 4 to (i) calculate the position

MSE for the path planning cost function, and (ii) calculate the largest eigenvalue of the position estimation error covariance for the path planning constraint.

5.1 Position MSE

The position MSE is a scalar measure, which accounts for the precision and bias of an estimator [32], and is commonly used due to its mathematical tractability. It refers to the mean of the squared estimation error in position at a specified location and time, i.e.,

$$\text{3-D position MSE} = \mathbb{E}\big[\boldsymbol{\Delta r}_r^{\mathsf{T}}\boldsymbol{\Delta r}_r\big]$$

$$= \text{tr}(\mathbb{E}[\boldsymbol{\Delta r}_r\boldsymbol{\Delta r}_r^{\mathsf{T}}])$$

$$= \text{tr}(\mathbb{E}[(\boldsymbol{\Delta r}_r' + \boldsymbol{r}_{r,\text{err}})(\boldsymbol{\Delta r}_r' + \boldsymbol{r}_{r,\text{err}})^{\mathsf{T}}])$$

$$= \text{tr}(\mathbb{E}[\boldsymbol{\Delta r}_r'\boldsymbol{\Delta r}_r'^{\mathsf{T}}]) + \|\boldsymbol{r}_{r,\text{err}}\|_2^2, \tag{5.2}$$

where $\mathbb{E}[\cdot]$ denotes the expected value and $\text{tr}(\cdot)$ denotes the trace, and (5.2) follows from $\boldsymbol{\Delta r}_r'$ being zero-mean. The position bias is $\|\boldsymbol{r}_{r,\text{err}}\|_2^2$, obtained from the first three elements of $\boldsymbol{x}_{r,\text{err}}$. The covariance of the unbiased position error is related to the weighted-position dilution of precision (WPDOP) [41, 63]

$$\text{WPDOP} \triangleq \sqrt{\text{tr}(\text{cov}[\boldsymbol{\Delta r}_r'])}$$

$$= \sqrt{h_{11}^2 + h_{22}^2 + h_{33}^2},$$

where h_{jj} is the j-th diagonal of $(\mathbf{H}^{\mathsf{T}}\mathbf{R}^{-1}\mathbf{H})^{-1}$.

The calculation of the position bias $\|\boldsymbol{r}_{r,\text{err}}\|_2$ due to multipath uses the simulated LOS and pseudorange bias due to multipath, which were found in the signal reliability maps. The steps to calculate the position MSE are described next.

5.1.1 Step 1: Create vector $\boldsymbol{b}$

For location p and time t, there are $\bar{N} \leq N$ reliable GNSS measurements as determined by the signal reliability maps such that for each $n = 1, \ldots, \bar{N}$ where t satisfies a time interval defined in $\mathcal{T}_{\text{SV}_{n},p}$. Also, there are $\bar{M} \leq M$ reliable cellular measurements for all $m = 1, \ldots, \bar{M}$, such that $b_{m,p}$ is not null and $|b_{m,p}| \leq \eta_m$, where η_m is the m-th element of $\mathbf{R}_a^{-\mathsf{T}} \mathbf{1}_{(\bar{N}+\bar{M}) \times 1} \eta_{\max}$, where $\mathbf{R}_a$ is the Cholesky factor of $\mathbf{R}$, that is, $\mathbf{R} = \mathbf{R}_a^{\mathsf{T}} \mathbf{R}_a$. The method for calculating the threshold $\eta_{\max}$ is shown in Section 5.2. The pseudorange bias vector is $\boldsymbol{b} = [\mathbf{0}_{1 \times \bar{N}}, b_{1,p}, \ldots, b_{\bar{M},p}]^{\mathsf{T}}$.

5.1.2 Step 2: Create Jacobian H

The rows of $\mathbf{H}$ are calculated from the transmitter positions of the corresponding elements in $\boldsymbol{b}$, and the coordinates of location p. It it is assumed that the biased position and true position are close enough so that the measurement Jacobian for the true position is close to that of the biased position.

5.1.3 Step 3: Calculate MSE

The position estimation MSE is calculated from

$$\text{3-D position MSE} \triangleq \text{WPDOP}^2 + \|\boldsymbol{r}_{r,\text{err}}\|_2^2.$$

The position MSE at a particular position p and time t, denoted $MSE(p,t)$, will be used in the path planning algorithm described in Chapter 6.

5.2 Uncertainty Constraint Calculation

This section describes the calculation of the path planning constraint: largest eigenvalue of the position estimation error covariance. The purpose of this constraint is to restrict the AGVs path to be within the maximum position uncertainty. To this end, the largest eigenvalue of the position-estimation error covariance will be used, which specifies the length of the largest axis of the uncertainty ellipsoid [61]. Methods for constraining the largest eigenvalue of a covariance matrix have been proposed in path planning literature [12, 25, 27, 48]. The largest eigenvalue at a particular position p and at time t, denoted $\lambda_{\max}(p, t)$, is found from the upper 3×3 matrix block of $(\mathbf{H}^\mathsf{T}\mathbf{R}^{-1}\mathbf{H})^{-1}$, where $\mathbf{H}$ is calculated according to the method discussed in Section 5.1.

This constraint is also related to a conservative upper bound on the position bias, which can be derived from the expression

$$\boldsymbol{r}_{r,\text{err}} = (\tilde{\mathbf{G}}^\mathsf{T}\tilde{\mathbf{G}})^{-1}\tilde{\mathbf{G}}^\mathsf{T}\bar{\boldsymbol{b}}, \tag{5.3}$$

where

$$\tilde{\mathbf{G}} = (\mathbf{I} - \bar{\mathbf{B}}\boldsymbol{\Gamma}\bar{\mathbf{B}}^\mathsf{T})\bar{\mathbf{G}}, \qquad \bar{\mathbf{G}} = \mathbf{R}_a^{-\mathsf{T}}\mathbf{G},$$

$$\boldsymbol{\Gamma} = (\bar{\mathbf{B}}^\mathsf{T}\bar{\mathbf{B}})^{-1}, \qquad \bar{\boldsymbol{b}} = \mathbf{R}_a^{-\mathsf{T}}\boldsymbol{b}, \qquad \bar{\mathbf{B}} = \mathbf{R}_a^{-\mathsf{T}}\mathbf{B}.$$

The derivation of (5.3) is given in Appendix A. The bias corresponding to the m-th cellular measurement is constrained such that $|b_{m,p}| \leq \eta_m$, where η_m is the m-th element of $\mathbf{R}_a^{-\mathsf{T}}\mathbf{1}_{(\bar{N}+\bar{M})\times 1}\eta_{\max}$ and $\eta_{\max}$ is the pseudorange bias threshold. The constraint can also be written as $|\bar{\boldsymbol{b}}| \leq \mathbf{1}_{(\bar{N}+\bar{M})\times 1}\eta_{\max}$, where $|\cdot|$ corresponds to the absolute value of each element in the vector.

Subsequently, the upper bound on the position bias can be found according to

$$\|\boldsymbol{r}_{r,\text{err}}\|_2 \leq \underset{|\bar{\boldsymbol{b}}| \leq \mathbf{1}\eta_{\max}}{\text{maximize}} \left\|(\tilde{\mathbf{G}}^\mathsf{T}\tilde{\mathbf{G}})^{-1}\tilde{\mathbf{G}}^\mathsf{T}\bar{\boldsymbol{b}}\right\|_2$$

$$\leq \underset{\|\bar{\boldsymbol{b}}\|_2 \leq \sqrt{\bar{M}}\eta_{\max}}{\text{maximize}} \left\|(\tilde{\mathbf{G}}^\mathsf{T}\tilde{\mathbf{G}})^{-1}\tilde{\mathbf{G}}^\mathsf{T}\bar{\boldsymbol{b}}\right\|_2 \tag{5.4}$$

$$= \underset{\|\bar{\boldsymbol{b}}\|_2 = \sqrt{\bar{M}}\eta_{\max}}{\text{maximize}} \left\|(\tilde{\mathbf{G}}^\mathsf{T}\tilde{\mathbf{G}})^{-1}\tilde{\mathbf{G}}^\mathsf{T}\bar{\boldsymbol{b}}\right\|_2 \tag{5.5}$$

$$= \sqrt{\bar{M}}\eta_{\max} \underset{\|\bar{\boldsymbol{b}}'\|_2 = 1}{\text{maximize}} \left\|(\tilde{\mathbf{G}}^\mathsf{T}\tilde{\mathbf{G}})^{-1}\tilde{\mathbf{G}}^\mathsf{T}\bar{\boldsymbol{b}}'\right\|_2 \tag{5.6}$$

$$= \eta_{\max}\sqrt{\bar{M}}\sigma'_{\max}\left[(\tilde{\mathbf{G}}^\mathsf{T}\tilde{\mathbf{G}})^{-1}\tilde{\mathbf{G}}^\mathsf{T}\right]$$

$$= \eta_{\max}\sqrt{\bar{M}\cdot\lambda_{\max}\left[(\tilde{\mathbf{G}}^\mathsf{T}\tilde{\mathbf{G}})^{-1}\right]} \triangleq \bar{r}_{\max}, \tag{5.7}$$

where $\sigma'_{\max}$ denotes the largest singular value, $\lambda_{\max}$ denotes the largest eigenvalue, and $\bar{r}_{\max}$ denotes the upper bound on the position bias. Equation (5.4) is found by relaxing the box constraint to a 2-norm ball where $\bar{M}$ is the number of cellular measurements used, (5.5) follows from convexity of the objective function (maximum of a convex function over convex constraints has an optimal solution on the extreme points of the constraints), and (5.6) is found through change of variables $\bar{\boldsymbol{b}}' \triangleq \frac{1}{\sqrt{\bar{M}}\eta_{\max}}\bar{\boldsymbol{b}}$. The term $\lambda_{\max}\left[(\tilde{\mathbf{G}}^\mathsf{T}\tilde{\mathbf{G}})^{-1}\right]$ denotes the maximum eigenvalue of the position estimation error covariance. The upper bound in (5.7) shows that the maximum eigenvalue also relates to the position error.

27

Chapter 6

Path Planning Generation

The path planning generation step prescribes an optimal path for the AGV to follow, utilizing the signal reliability maps. This chapter describes the steps to determine the optimal path between a start position at a desired departure time and a target position. The optimal path is one that accounts for the shortest path length, the position MSE, and the maximum tolerable uncertainty (as measured by the largest eigenvalue of the position estimation error covariance).

To account for both position error and path length, the optimization cost function is chosen to be the sum of the position MSE along the path, multiplied by the distance between two adjacent points. The distance is explicitly considered in the cost function because only including position MSE could result in lengthy paths, e.g., paths that require the AGV to leave and re-enter the urban environment. The optimization function constraints account for the position bias due to cellular multipath and uncertainty about the AGVs position estimate. The user-specified constraints are: (i) threshold for position bias $\bar{r}_{\max}$

and (ii) threshold for position uncertainty $\bar{\lambda}_{\text{max}}$. The threshold $\bar{\lambda}_{\text{max}}$ is used as a constraint for all points p and time t along the AGVs path, i.e., $\lambda_{\text{max}}(p,t) \leq \bar{\lambda}_{\text{max}}$. The threshold $\bar{\lambda}_{\text{max}}$ is also used along with $\bar{r}_{\text{max}}$ to calculate a threshold on the pseudorange bias η_{max}. The calculation of η_{max} can be achieved from (5.7) by substituting the user specified $\bar{r}_{\text{max}}$, and using $\bar{\lambda}_{max}$ in place of $\lambda_{\text{max}}\left[(\tilde{\mathbf{G}}^{\mathsf{T}}\tilde{\mathbf{G}})^{-1}\right]$. Since $\bar{M} \leq M$, $\bar{M}$ is replaced with M to calculate an upper bound that is independent of a particular location and is valid for the entire environment.

The path planning generation block solves a constrained optimization problem, discussed next, and returns the AGVs prescribed path along with a list of reliable GNSS satellites and cellular towers to use along the path. As the AGV executes this optimal path, it only uses signals from these reliable GNSS satellites and cellular towers. Note that to make the WNLS estimation problem observable, there needs to be at least either (i) $\bar{N} \geq 4$ reliable GNSS satellite signals to estimate $\boldsymbol{x}'_r \triangleq \left[\boldsymbol{r}_r^{\mathsf{T}}, c\delta t_r\right]^{\mathsf{T}}$ or (ii) $\bar{N} + \bar{M} \geq 5$ reliable GNSS satellite and cellular signals to estimate $\boldsymbol{x}_r \triangleq \left[\boldsymbol{r}_r^{\mathsf{T}}, c\delta t_r, c\delta t_{\text{SOP},1}\right]^{\mathsf{T}}$, with $\bar{M} \geq 1$. Fig. 6.1 summarizes the flowchart of signal reliability map generation, position MSE and eigenvalue calculation, and path planning generation with the corresponding inputs and outputs defined in Chapters 4 and 5.

To account for distance in the optimization problem, each location p is assigned a distance, for $p = 1, \ldots, P$. This distance, denoted $dist(p)$, signifies the length of the road network segment represented by the location p and its adjacent location, and is based on the spatial discretization of the reliability maps. The steps to calculate the distance for locations $p = 1, \ldots P$ are summarized in Fig. 6.2. Point p_3 in Fig. 6.2 shows the calculation
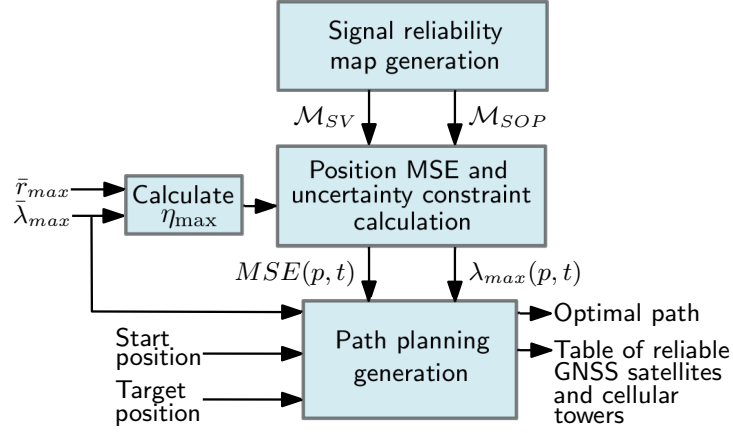
Figure 6.1: Flow chart of signal reliability map generation, position MSE and uncertainty constraint calculation, and path planning generation.

of $dist(p_3)$ when the point is adjacent to an intersection, and Point p_2 in Fig. 6.2 shows the calculation of $dist(p_2)$ when the point is not adjacent to an intersection.
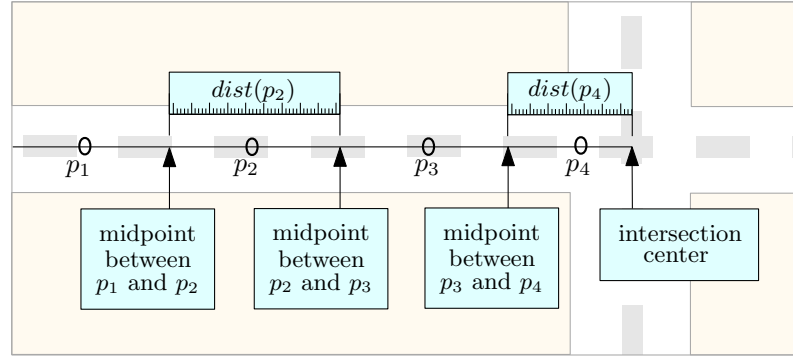
Figure 6.2: Steps to calculate $dist(p)$ for 3-D points whose indices are p_2 and p_4. For p_4, which is adjacent to an intersection, the 3-D midpoint between p_4 and p_3 is calculated in, then $dist(p_4)$ is the distance between the midpoint and the intersection center. For p_2 which is not adjacent to an intersection, the midpoint between p_3 and p_2 is calculated, then the midpoint between p_2 and p_1 is calculated. Then, $dist(p_2)$ is the distance between the two calculated midpoints.

The path planning optimization problem is formatted next. Formally, a path from the start to the target location is denoted $\pi \in \mathcal{P}$, where $\mathcal{P}$ is the set of all paths. The path π is composed of a sequence of position indices between the start position index p_s and

30

the target p_g, namely $\pi = \{p_s, p_1, p_2, \ldots, p_g\}$. To simplify the optimization problem and subsequently the path planning algorithm, it will be assumed that the GNSS reliability map from the departure time through the time the AGV arrives at the target position is the same, making $MSE(p,t) = MSE(p)$ and $\lambda_{\max}(p,t) = \lambda_{\max}(p)$. This assumption is reasonable for short AGV paths during which the geometry of the GNSS satellite constellation does not vary significantly. For example, the GPS satellite moves by approximately $3.57°$ in 15 minutes (see Appendix B).

The optimization problem is expressed as

$$\underset{\pi \in \mathcal{P}}{\text{minimize}} \quad \sum_{p \in \pi} dist(p) \cdot MSE(p)$$

$$\text{subject to} \quad \lambda_{\max}\left[(\tilde{\mathbf{G}}^\mathsf{T}\tilde{\mathbf{G}})^{-1}\right] \leq \bar{\lambda}_{\max}$$

$$\|\boldsymbol{r}_{r,\text{err}}\|_2 \leq \bar{r}_{\max}.$$

From (5.7), the second constraint can be formulated to yield the optimization problem

$$\underset{\pi \in \mathcal{P}}{\text{minimize}} \quad \sum_{p \in \pi} dist(p) \cdot MSE(p) \qquad (6.1)$$

$$\text{subject to} \quad \lambda_{\max}\left[(\tilde{\mathbf{G}}^\mathsf{T}\tilde{\mathbf{G}})^{-1}\right] \leq \bar{\lambda}_{\max}$$

$$|\bar{\boldsymbol{b}}| \leq \mathbf{1}\eta_{\max}.$$

Note that the cost function accounts for both the position MSE and the path length. Other cost functions could be used to favor either part: position MSE versus path length, e.g., using an exponential for either term.

The optimization problem (6.1) resembles the problem of finding the shortest path in a weighted graph, where the roads are the edges of the graph and the path planning

metric determines the weight of each edge. Several algorithms have been proposed to find the shortest path [14, 17, 59]. Among these algorithms, Dijkstra's algorithm is most widely used and is recognized as a classic algorithm to find the shortest path between two arbitrary nodes of a weighted graph [67, 68]. Dijkstra's algorithm is readily implementable with acceptable complexity; thus it is adopted in this thesis to solve the AGV path planning problem.

Assume that the AGV is driving in a region consisting of ι intersections and ω roads (e.g., side streets and highways). This region can be modeled by a graph $\mathcal{G} = (\iota, \omega)$ which consists of ι nodes and ω edges. The path planning metric $f(\beta, \alpha)$ assigns a non-negative real number corresponding to the weight of the edge from nodes β to α in $\mathcal{G}$. Based on the objective function in (6.1), the weight is given by the position MSE at all points from nodes β and α, denoted $P(\beta, \alpha)$, multiplied by $dist(p)$, i.e.,

$$f(\beta, \alpha) = \sum_{p \in P(\beta, \alpha)} dist(p) \cdot MSE(p).$$

It is assumed that the deviation between $MSE(p)$ and the MSE calculated at the true time is small. Based on the constraints in (6.1), if $\lambda_{\max}(p)$ exceeds $\bar{\lambda}_{\max}$ for $p \in P(\beta, \alpha)$, then the edge is removed from the graph.

Dijkstra's algorithm is implemented as follows. Let s indicate the start node at which the AGV starts, and let g indicate some target node. Let $d(g)$ denote the cost along the path from s to g, let S denote the set of edges that have already been evaluated by the algorithm, and let V denote the set of unvisited nodes. Within a path $\gamma(g) \in \mathcal{G}$, denote α_p as the predecessor of α and β_p as the predecessor of β. The path planning is initialized as follows

- $d(s) = 0$

- For each node α adjacent to s, set $d(\alpha) = f(s, \alpha)$ and $\alpha_p = s$

- For each node α such that $\alpha \neq s$ and α in not adjacent to s, set $d(\alpha) = \infty$

- $S = \{s\}$

After the above initialization, the path planning algorithm outlined in Algorithm 1 is executed.

Algorithm 1 $Input :$ $\mathcal{G}$, s, g, S, and $f(\beta, \alpha)$

Output : $d(g)$ *and* $\gamma(g)$

Find $\alpha \in V$ that minimizes $d(\alpha)$

For each β adjacent to α

   If $d(\alpha) + f(\beta, \alpha) < d(\beta)$,

      $d(\beta) = d(\alpha) + f(\beta, \alpha)$

      $\beta_p = \alpha$

   Else,

      Do not change $d(\beta)$ and β_p

   End if

End for

$V \leftarrow V - \{\alpha\}$

$S \leftarrow S + \{\alpha\}$

If $S \neq V$,

   Goto Step 1

Else,

    Exit the Algorithm

End if

        The node and edge data of the graph $\mathcal{G}$ can be extracted from digital maps, such as the Open Street Map (OSM) database [7]. OSM is built by a community of mappers that contribute and maintain roads, trails, and railway stations information.

Chapter 7

Simulation Results

This chapter presents simulation results evaluating the performance of the AGV path planning approach developed in Chapters 3–6. The following sections describes the simulation environment setup. Next, the simulation results are presented and discussed.

7.1 Simulation Setup and Scenario Description

The simulation environment considered downtown Riverside, California, USA. A 3-D building map of this environment was obtained from ArcGIS online [2]. The GNSS satellite constellation considered comprised GPS and Galileo satellites, and the GNSS signal reliability maps were generated using the method described in Section 4.1. Fig. 7.1 illustrates the GNSS satellites' skyplot over Riverside at time $t = 8:00$ pm, coordinated universal time (UTC), on August 23, 2018. The elevation and azimuth angles for both GPS and Galileo satellites were obtained using the PyEphem Python library [8]. Satellites with an elevation angle less than 15 degrees were not used, as signals from these satellites tend

to be severely degraded due to ionosphere, troposphere, and multipath.
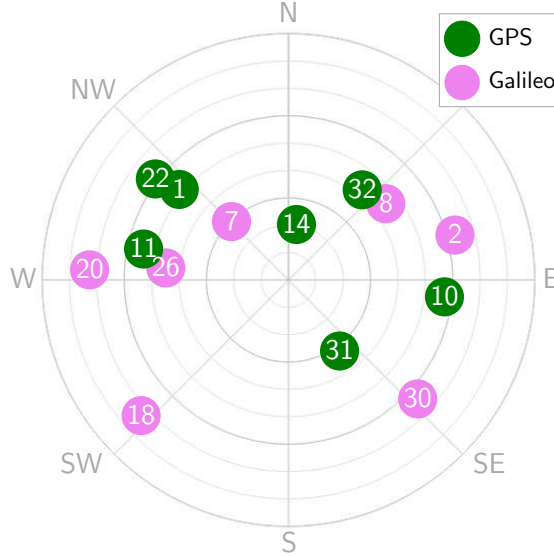
Figure 7.1: Skyplot of GNSS satellites over Riverside, California, USA, at 8:00 pm, August 23, 2018. The skyplot shows the elevation and azimuth angles of GNSS satellites. The green and the pink circles correspond to GPS and Galileo satellites respectively. The numbers correspond to the pseudorandom noise (PRN) code for each satellite [15, 45]. Data source: [4].

Fig. 7.2 illustrates the simulation environment, the start and target points, and the location of the cellular towers. Signals from four cellular towers were simulated: three towers located inside the downtown area and one tower located outside the downtown area. The Wireless Insite X3D model [9] was used to simulate the cellular towers and to generate the complex channel impulse response on a grid of receiver locations. The channel impulse response was used to calculate pseudorange bias $b_{m,p}$ according to (4.4) for each cellular tower and each grid point p. The simulation settings are summarized in Table 7.1.

The position MSE and largest eigenvalue of the position estimation error covari-
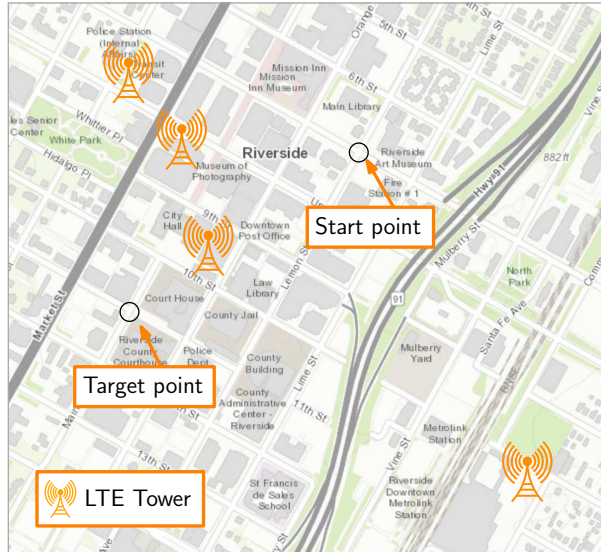
Figure 7.2: Simulation environment showing the start and target points and location of three cellular transmitters. This figure is obtained with ArcGIS® [3].

ance were calculated from the GNSS and cellular reliability maps as described in Chapter 5 and Dijkstra's algorithm was implemented to find the AGVs optimal path as discussed in Chapter 6.

Two AGVs were considered to be present in the urban environment. Both AGVs had the same start position, target position, time of departure, and the optimization problem for each AGV used the same threshold values $\bar{\lambda}_{\max}$ and $\bar{r}_{\max}$. AGV A was equipped with only GPS and Galileo receivers, while AGV B was equipped with GPS, Galileo, and cellular LTE receivers.

Two simulation scenarios were conducted, where each scenario considered a different choice for thresholds. The simulation results for each scenario are presented next.

Table 7.1: Simulation Settings

Parameter	Definition	Value
N	Number of GNSS satellites	14
M	Number of cellular towers	4
t	Time in UTC	August 23, 2018, 8:00 pm
$\{\sigma_{\mathrm{SV,n}}^2\}_{n=1}^N$	GNSS measurement noise variance	5 m^2
$\{\sigma_{\mathrm{SOP,m}}^2\}_{m=1}^M$	Cellular measurement noise variance	5 m^2

7.2 Simulation Results

7.2.1 Scenario 1

Table 7.2 shows the thresholds used for both AGV A and AGV B. As discussed in Chapters 5–6, the user-specified thresholds are $\bar{r}_{\mathrm{max}}$ and $\bar{\lambda}_{\mathrm{max}}$, from which η_{max} is computed according to (5.7), and η_m corresponds to the m-th element of $\mathbf{R}_a^{-\mathsf{T}}\mathbf{1}_{(\bar{N}+\bar{M})\times 1}\eta_{\mathrm{max}}$.

Table 7.2: Scenario 1 Thresholds

Parameter	Definition	Value
$\bar{r}_{max}$	Position bias threshold	4 m
$\bar{\lambda}_{max}$	Eigenvalue constraint threshold	4 m^2
η_{max}	Pseudorange error threshold	1 m
η_m	Weighted pseudorange error threshold	$\sqrt{5}$ m

For the given simulation settings, AGV A had no feasible path which satisfies the

constraints. One path was returned by the proposed algorithm by relaxing the eigenvalue constraint to $\bar{\lambda}_{\max} = 4.44$ m^2. Fig. 7.3 (a) illustrates this path, while Table 7.3 presents its distance, total RMSE, maximum eigenvalue, and the cost function value. For a given path π, the total RMSE was calculated according to

$$\text{Total RMSE} = \sqrt{\frac{\sum\limits_{p \in \pi} MSE(p)}{h(\pi)}},$$

where $h(\cdot)$ denotes the number of locations in the path π. In contrast, AGV B had four feasible paths without the need to relax the eigenvalue constraint (i.e., with $\bar{\lambda}_{\max} = 4$), with Path B1 being the optimal path. Fig. 7.3 (b) illustrates these paths and Table 7.3 compares them.

Table 7.3: Scenario 1 Results

	Path	Distance	Total RMSE	Maximum eigenvalue	Cost function value
AGV A	Path A1	1006 m	4.37 m	4.44 m^2	16397
AGV B	Path B1	995 m	3.91 m	3.53 m^2	13108
	Path B2	1016 m	3.91 m	3.74 m^2	13158
	Path B3	1006 m	3.95 m	3.91 m^2	13358
	Path B4	1004 m	3.96 m	3.74 m^2	13408

The following can be concluded from the above results. First, including cellular LTE signals made the optimization problem feasible, without having to relax the constraint. Second, including cellular LTE signals resulted in several feasible paths to choose from (besides the optimal path), which could be useful if other considerations arise, e.g., traffic

jams and road blockages due to construction. Third, while the optimal path ended up yielding the shortest distance together with the total RMSE, a tradeoff between the shortest path and the total RMSE can be seen in the other feasible paths (e.g., Path B2 has lower total RMSE than Path B3 but has longer distance).
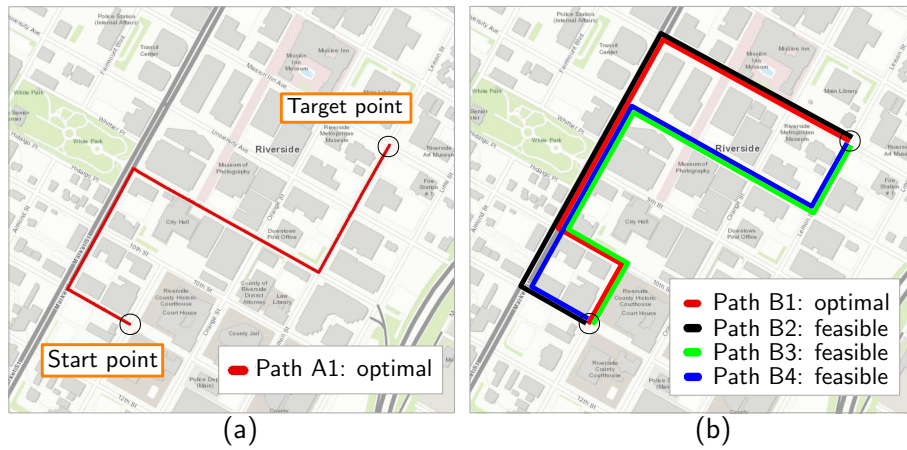
Figure 7.3: Simulation results for Scenario 1. (a) The optimal path for AGV A, generated after relaxing the eigenvalue constraint from $\bar{\lambda}_{\max} = 4$ to $\bar{\lambda}_{\max} = 4.44$. (b) The optimal path and three feasible paths for AGV B without relaxing the eigenvalue constraint (i.e., with $\bar{\lambda}_{\max} = 4$). The optimal path Path B1 was shorter and produced less total RMSE than all other paths: Path A1, Path B2, Path B3, and Path B4. This figure is obtained with ArcGIS® [3].

7.2.2   Scenario 2

This scenario is similar to Scenario 1, except that the eigenvalue constraint is relaxed even further to obtain several feasible paths for AGV A. Table 7.4 shows the new thresholds used for both AGV A and AGV B.

By changing the constraints from Scenario 1, the number of feasible paths for AGV A increased from zero to two. Fig. 7.4 (a) illustrates these paths, while in Table 7.5

Table 7.4: Scenario 2 Thresholds

Parameter	Definition	Value
$\bar{r}_{max}$	Position bias threshold	4 m
$\bar{\lambda}_{max}$	Eigenvalue constraint threshold	5 m^2
$\eta_{\max}$	Pseudorange error threshold	$\frac{2}{\sqrt{5}}$
η_m	Weighted pseudorange error threshold	2

compares them. In contrast, the number of feasible paths for AGV B increased from four to twelve possible paths, Fig. 7.4 (b)–(d) illustrates all these paths and Table 7.5 compares them.

The following can be concluded from the above results. First, while both AGV A and AGV B found optimal and feasible paths, the optimal path for AGV B was significantly shorter than that for AGV A. Hence, utilizing cellular signals "opened up" areas in the environment that were otherwise infeasible with GNSS only. Second, slightly relaxing the constraint resulted in many new feasible paths versus Scenario 1, with the optimal path Path B1 in Scenario 2 being reasonably shorter than the optimal path in Scenario 1 (namely, 33% shorter) with a slightly larger RMSE (namely, 11% higher).

Table 7.5: Scenario 2 Results

	Path	Distance	Total RMSE	Maximum eigenvalue	Cost Function Value
AGV A	Path A1	1006 m	4.37 m	4.44 m^2	16397
	Path A2	1013 m	4.44 m	4.44 m^2	17012
AGV B	Path B1	748 m	4.34 m	4.28 m^2	11724
	Path B2	995 m	3.91 m	3.53 m^2	13108
	Path B3	1016 m	3.91 m	3.74 m^2	13158
	Path B4	1006 m	3.95 m	3.74 m^2	13358
	Path B5	1004 m	3.95 m	3.74 m^2	13408
	Path B6	1013 m	3.97 m	4.28 m^2	13412
	Path B7	1006 m	3.97 m	4.28 m^2	13462
	Path B8	1014 m	4.17 m	4.28 m^2	14605
	Path B9	1493 m	4.08 m	4.20 m^2	21519
	Path B10	1491 m	4.18 m	4.28 m^2	22515
	Path B11	1750 m	4.11 m	4.28 m^2	24401
	Path B12	1756 m	4.11 m	4.28 m^2	25397
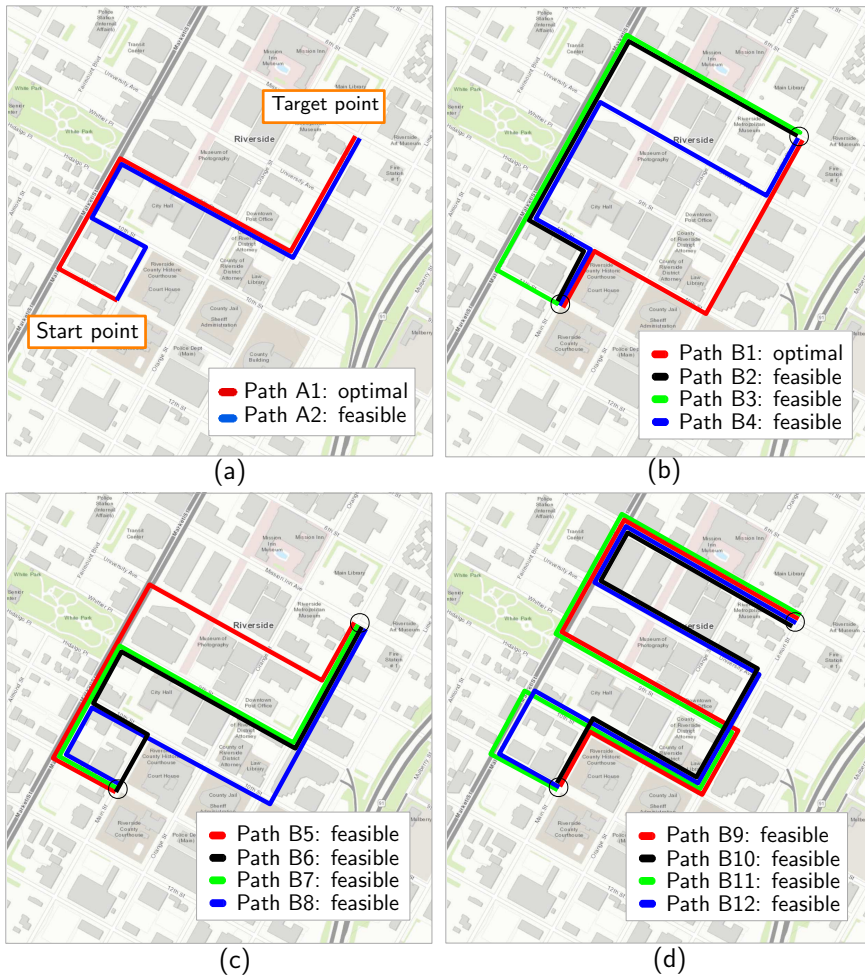
Figure 7.4: Simulation results for Scenario 2. (a) The feasible paths for AGV A, where Path A1 is the optimal path. (b) Four feasible paths for AGV B which produced the lowest cost function, i.e., Paths B1 – B4. (c) Paths B5 – B8 for AGV B in order of lowest to highest cost function value. (d) Paths B9 – B12 for AGV B in order of lowest to highest cost function value. This figure is obtained with ArcGIS® [3].

Chapter 8

Experimental Results

This chapter presents experimental results for ground vehicle path planning in an urban environment with real GPS and cellular LTE singals. The next section describes the experimental setup and the scenarios considered and the following section discusses the obtained results.

8.1   Experimental Setup and Scenario Description

A vehicle was equipped with a consumer-grade cellular omnidirectional Laird antenna to receive cellular LTE signals [5]. The signals were down-mixed and sampled using a National Instruments (NI) dual-channel universal software radio peripheral (USRP)– 2954R®, driven by a GPS-disciplined oscillator (GPSDO) [6]. The vehicle was also equipped with a Septentrio AsteRx-i V® integrated GNSS-IMU module, which is equipped with a dual antenna, multi-frequency GNSS receiver and a Vectornav VN-100 micro-electromechanical system (MEMS) inertial measurement unit (IMU). Septentrio's post-processing software

development kit (PP-SDK) was used to process carrier phase observables collected by the AsteRx-i V® and by a nearby differential GPS base station to obtain a carrier phase-based navigation solution. This integrated GNSS-IMU real-time kinematic (RTK) system was used to produce the vehicle's ground truth path. The GNSS receiver also produced GNSS pseudorange measurements, which were used as discussed in Chapters 3 – 4. The experimental setup is shown in Fig. 8.1.
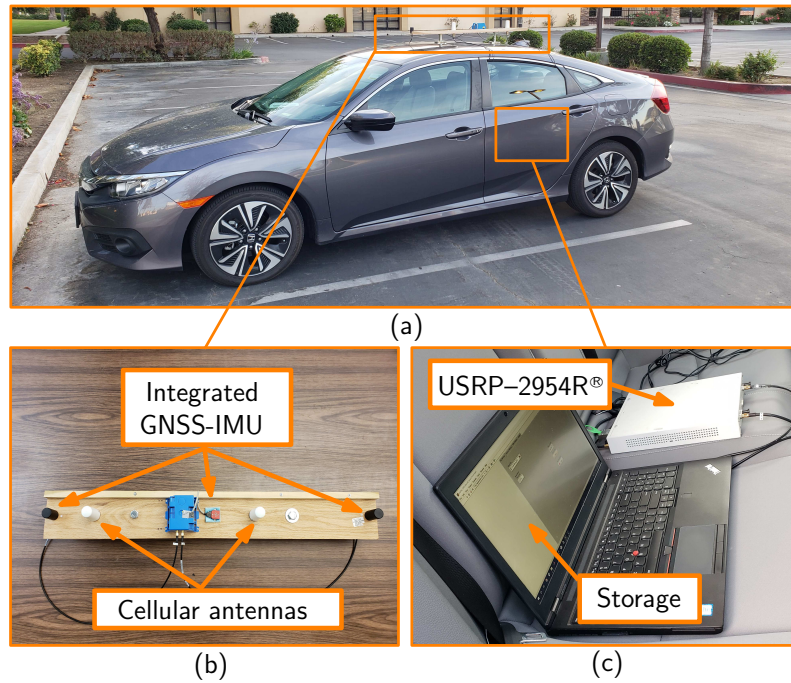
Figure 8.1: Experiment setup. (a) A depiction of the vehicle used to conduct the experiment, which was equipped with the AsteRx-i V® GNSS-IMU module, antennas, USRP–2954R®, and laptop for storage and processing. (b) The setup mounted on top of the vehicle. (c) The setup placed inside the vehicle.

The experiment was conducted in downtown Riverside, California, U.S.A. Eight GPS satellites were present at the time of the experiment and four LTE towers were used. The characteristics of the four LTE towers are summarized in Table 8.1 and their locations

are depicted in Fig. 8.2.

Table 8.1: Characteristics of the LTE Towers

Tower	Service provider	Carrier frequency (MHz)	Cell ID	Bandwidth (MHz)
1	AT&T	1955	219	20
2	AT&T	1955	348-350	20
3	Verizon	2145	392	20
4	Verizon	2145	79	20

Due to the hardware setup used in the experiment, the GPS receiver and LTE receiver clocks were not synchronized, which implies that each receiver has a different clock bias, denoted $\delta t_{r_{\mathrm{SV}}}$ and $\delta t_{r_{\mathrm{SOP}}}$, respectively. To account for this, the GPS receiver's clock bias in (3.1), namely $\delta t_{r_{\mathrm{SV}}}$, was included into the state $\boldsymbol{x}_r$, while the difference between the LTE receiver's clock bias and the first LTE tower's clock bias, namely $(\delta t_{r_{\mathrm{SOP}}} - \delta t_{\mathrm{SOP},1})$ was included in the state $\boldsymbol{x}_r$. Therefore, the state vector that was estimated was $\boldsymbol{x}_r = \left[\boldsymbol{r}_r^{\mathsf{T}}, c\delta t_{r_{\mathrm{SV}}}, c(\delta t_{r_{\mathrm{SOP}}} - \delta t_{\mathrm{SOP},1})\right]^{\mathsf{T}}$. The matrix $\mathbf{B}$ in (3.5) was adjusted in accordance with this new state to

$$\mathbf{B} \triangleq \begin{bmatrix} \mathbf{1}_{N\times 1} & \mathbf{0}_{N\times 1} \\ \mathbf{0}_{M\times 1} & \mathbf{1}_{M\times 1} \end{bmatrix}. \tag{8.1}$$

Fig. 8.3 depicts the start and target points for the ground vehicle. The path planning approach described in Chapters 7 was performed offline with the settings in Table 8.2. The LTE measurement noise variances were calculated using the sample variance

46
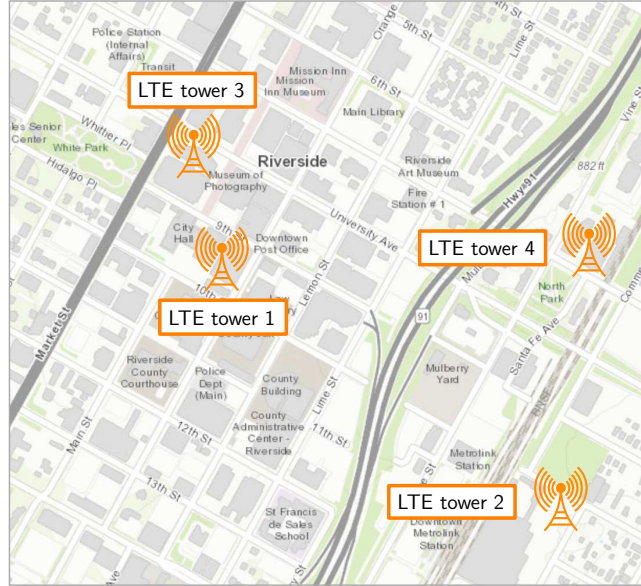
Figure 8.2: Location of four LTE towers in downtown Riverside, California, whose signals were used. This figure is obtained with ArcGIS® [3].

from received pseudoranges, while the vehicle was stationary over $K = 100$ samples. The perturbation parameters $\hat{\epsilon}_m$ and $\widehat{\sigma^2_{\epsilon,m}}$ were also calculated, while the vehicle was stationary over $K = 10$ samples. The path planning generator returned an optimal path and a feasible path depicted in Fig. 8.3. Also shown in Fig. 8.3 is the shortest path (not returned by the path planning generator), but that will be analyzed.

Next, the experimental results for two scenarios are presented. The first scenario compares the experimental navigation performance versus the navigation performance predicted by the offline path planning generator. The second scenario evaluates the navigation performance if the vehicle chooses to take the shortest path (path 3) instead of the optimal or feasible path.
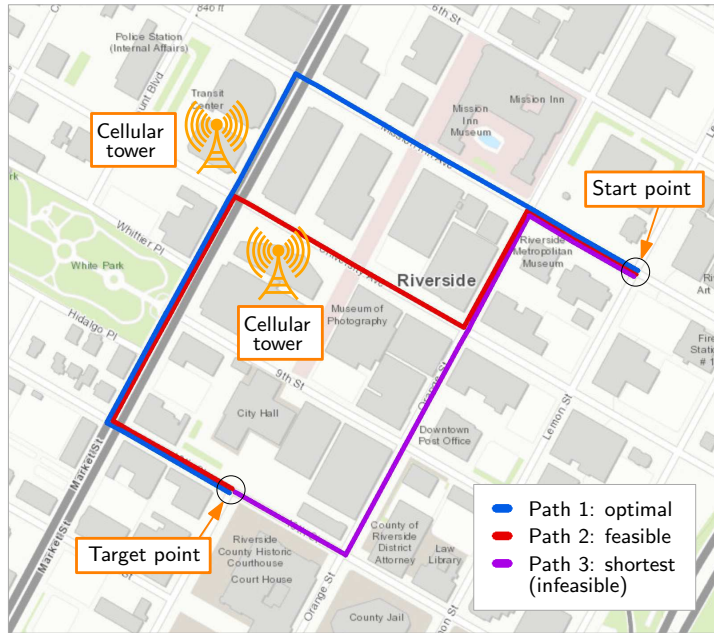
Figure 8.3: The optimal path and feasible path returned by the path planning generator. Path 3 is the shortest path between the start and target points but is infeasible as it violates the constraints. This figure is obtained with ArcGIS® [3].

8.2 Experimental Results

8.2.1 Scenario 1

The purpose of this scenario is to compare the simulated path planning navigation results with the experimental navigation results. Table 8.3 compares the navigation performance along the optimal and feasible paths returned by the simulated results versus those returned experimentally.

Note the close match between the simulated and experimental navigation performance. In particular despite the differences in the simulated and experimental cost function values, path 1 was still the optimal path *experimentally*.

The simulated RMSE at each location and the actual RMSE are compared in Fig.

Table 8.2: Experiment Settings

Parameter	Definition	Value
N	Number of satellites	8
M	Number of cellular towers	4
t	Start time (UTC)	August 24st, 2018, 6:34 am
$\bar{r}_{max}$	Position bias threshold	15 m
$\bar{\lambda}_{max}$	Eigenvalue constraint threshold	30 m^2
$\eta_{\max}$	Pseudorange error threshold	$\frac{2}{\sqrt{10}}$
K	Number of cellular measurements used for initialization	10
$\{\sigma^2_{\text{SV,n}}\}_{n=1}^{N}$	GNSS measurement noise variance	$\{7.1, 5.1, 3.9,$ $6.9, 7.1, 6.7,$ $5.8, 9.5\}$ m^2
$\{\sigma^2_{\text{SOP,m}}\}_{m=1}^{M}$	Cellular measurement noise variance	$\{8.7, 4.4, 7.8,$ $4.6\}$ m^2

8.4. Also shown in Fig. 8.4 are the vehicle's ground truth path versus the path estimated with GNSS and cellular LTE signals. From Fig. 8.4, it can be seen that the simulated RMSE closely follows the experimentally estimated path. However, in one particular area (depicted with a dashed circle), the experimental RMSE was 9.51 m, while the simulated RMSE at that area was smaller than 5 m. This may be due to the fact that the simulator does not account for attenuation due to trees (there is dense foliage near the area). This result reveals that accurate knowledge of the environment is crucial for accurately simulating the position MSE. The foliage was not included in the 3-D map because it was not surveyed or

Table 8.3: Simulated and experimental navigation results along optimal and feasible paths

Path	Path length		Total RMSE	
	Simulation	Experiment	Simulation	Experiment
Path 1: optimal	872 m	878 m	6.55 m	6.63 m
Path 2: feasible	884 m	886 m	7.19 m	7.47 m

Path	Maximum eigenvalue		Cost function value	
	Simulation	Experiment	Simulation	Experiment
Path 1: optimal	27.91 m^2	27.27 m^2	55939	42216
Path 2: feasible	27.91 m^2	26.85 m^2	68688	60029

available online prior to the experiment. However, existing software packages (e.g., Wireless Insite) could simulate foliage effects.

8.2.2 Scenario 2

This scenario evaluates the navigation performance when the vehicle does not traverse any of the paths returned by the path planning generator, and instead executes the path with the shortest length, namely path 3 in Fig. 8.3, which has a corresponding distance of 629 m between the start and target points. As shown in Fig. 8.5, path 3 was deemed infeasible by the path planning generator as several areas had a simulated RMSE over 20 m, and one area had an insufficient number of measurements to produce an estimate for $\boldsymbol{x}_r$.

The experimental RMSE along the entire path was 12.12 m in areas where the
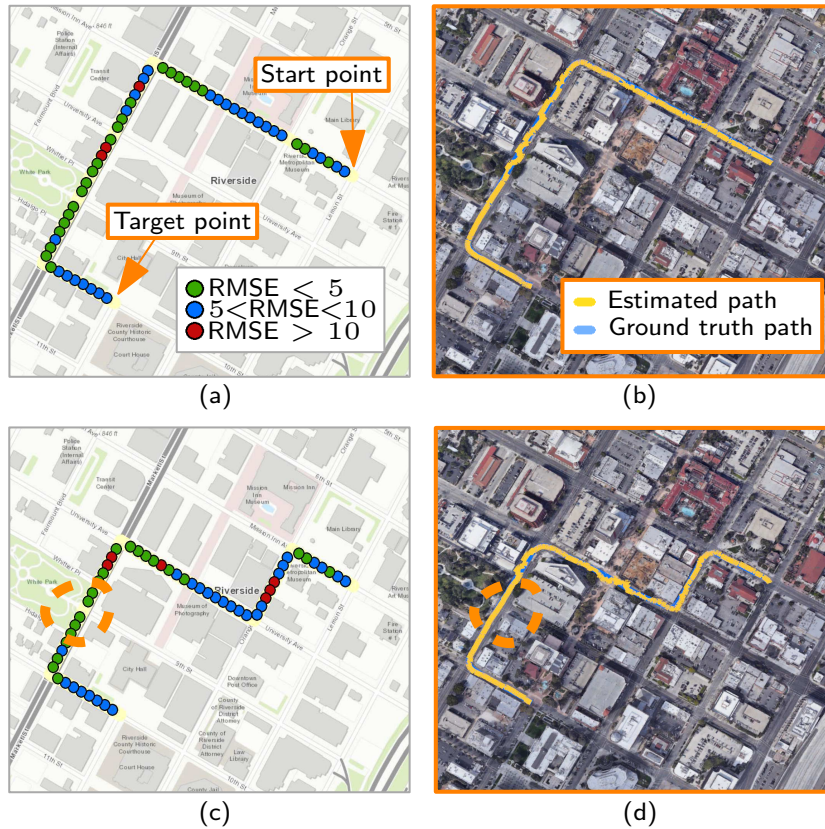
Figure 8.4: Simulated and experimental results along the optimal path (a), (b) and feasible path (c), (d). Here, (a), (c) show the simulated RMSE values at locations along the path, while (b), (d) compare the vehicle's experimentally estimated path from GNSS and cellular signals versus the ground truth path from the GNSS-IMU with RTK module. This figure is obtained with ArcGIS® [3].

navigation solution was computed, which is twice as large as the position RMSE of the other two paths. The dashed circle depicted in Fig. 8.5 (b) shows the area where the vehicle was unable to estimate its position from GNSS and cellular signals, which is consistent with Fig. 8.5 (a). The result in this scenario highlights the importance of planning the path of an AGV to avoid situations where the AGV could not estimate its state.
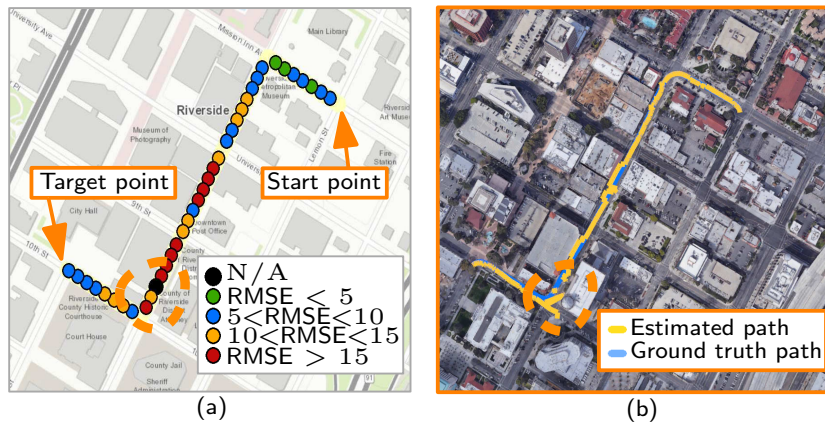
Figure 8.5: Simulated and experimental results along the shortest (but infeasible) path. Here (a) shows the simulated RMSE values, while (b) compares the vehicle's experimentally estimated path from GNSS and cellular measurements. The dashed circle in (a) specifies the area in which the simulator did not have a sufficient number of measurements to estimate the vehicle's position (corresponding to an RMSE of N/A), which matches the same area in (b) at which there weren't sufficient pseudorange measurements from GNSS and cellular signals to estimate the vehicles's position. This figure is obtained with ArcGIS® [3].

Chapter 9

Conclusions

This thesis considers the problem where an AGV equipped with GNSS and cellular receivers desires to reach a target location while taking the shortest path and optimizing over position MSE, while guaranteeing that the bias in the position estimate and the position uncertainty are below a desired threshold. A path planning generator prescribes a trajectory that satisfies this objective using a 3-D building map to create signal reliability maps for GNSS and cellular LTE signals. The signal reliability maps are used to calculate the position MSE and uncertainty-based constraint at each location, which in turn is used to generate an optimal path for the AGV to follow. A simulation compared the feasible paths given by the path planning generator for a vehicle that uses GNSS and cellular signals versus GNSS only. The simulation results demonstrated that utilizing cellular signals "opened up" areas in the environment that were otherwise infeasible with GNSS only. Experimental results showed an improvement in the position RMSE when choosing the prescribed path instead of an alternate path, and that the simulated results were consistent with the experimental results

when the environment is known accurately. Also, results were shown for when the AGV does not use the proposed algorithm and instead takes the shortest path, and demonstrates the importance of path planning for AGVs to avoid situations where the AGV cannot estimate its state.

Appendix A

Relationship between Pseudorange and Position Bias

This appendix is to establish the relationship between position bias and pseudorange bias. For this analysis, it is assumed that the biased position and true position are close enough so that the measurement Jacobians evaluated at each are approximately equal.

From (5.1), the relationship between pseudorange bias and the state bias is given by

$$\boldsymbol{x}_{r,err} \triangleq (\mathbf{H}^\mathsf{T}\mathbf{R}^{-1}\mathbf{H})^{-1}\mathbf{H}^\mathsf{T}\mathbf{R}^{-1}\boldsymbol{b}.$$

Consider the Choleky factorization of $\mathbf{R} = \mathbf{R}_a^\mathsf{T}\mathbf{R}_a$, and define $\bar{\mathbf{H}} \triangleq \mathbf{R}_a^{-\mathsf{T}}\mathbf{H}$ and $\bar{\boldsymbol{b}} \triangleq \mathbf{R}_a^{-\mathsf{T}}\boldsymbol{b}$, which results in

$$\boldsymbol{x}_{r,err} = (\bar{\mathbf{H}}^\mathsf{T}\bar{\mathbf{H}})^{-1}\bar{\mathbf{H}}^\mathsf{T}\bar{\boldsymbol{b}}. \tag{A.1}$$

Recall that $\mathbf{H} \triangleq [\mathbf{G}, \mathbf{B}]$ and $\boldsymbol{x}_{r,\mathrm{err}} \triangleq [\boldsymbol{r}_{r,\mathrm{err}}^\mathsf{T}, c\boldsymbol{\delta t}_{\mathrm{err}}^\mathsf{T}]^\mathsf{T}$; therefore, (A.1) can be partitioned as

$$
\begin{bmatrix} \boldsymbol{r}_{r,\mathrm{err}} \\ c\boldsymbol{\delta t}_{\mathrm{err}} \end{bmatrix} = \begin{bmatrix} \bar{\mathbf{G}}^\mathsf{T}\bar{\mathbf{G}} & \bar{\mathbf{G}}^\mathsf{T}\bar{\mathbf{B}} \\ \bar{\mathbf{B}}^\mathsf{T}\bar{\mathbf{G}} & \bar{\mathbf{B}}^\mathsf{T}\bar{\mathbf{B}} \end{bmatrix}^{-1} \begin{bmatrix} \bar{\mathbf{G}}^\mathsf{T} \\ \bar{\mathbf{B}}^\mathsf{T} \end{bmatrix} \bar{\boldsymbol{b}}.
$$

An expression for $\boldsymbol{r}_{r,\mathrm{err}}$ can be found through block matrix inversion

$$
\boldsymbol{r}_{r,\mathrm{err}} = \begin{bmatrix} \mathbf{A} & -\mathbf{A}\bar{\mathbf{G}}^\mathsf{T}\bar{\mathbf{B}}\boldsymbol{\Gamma} \end{bmatrix} \begin{bmatrix} \bar{\mathbf{G}}^\mathsf{T} \\ \bar{\mathbf{B}}^\mathsf{T} \end{bmatrix} \bar{\boldsymbol{b}}, \tag{A.2}
$$

$$
\mathbf{A} \triangleq (\bar{\mathbf{G}}^\mathsf{T}\bar{\mathbf{G}} - \bar{\mathbf{G}}^\mathsf{T}\bar{\mathbf{B}}\boldsymbol{\Gamma}\bar{\mathbf{B}}^\mathsf{T}\bar{\mathbf{G}})^{-1},
$$

where $\boldsymbol{\Gamma} = (\bar{\mathbf{B}}^\mathsf{T}\bar{\mathbf{B}})^{-1}$. After rearranging (A.2), the relationship is found to be

$$
\boldsymbol{r}_{r,\mathrm{err}} = (\bar{\mathbf{G}}^\mathsf{T}\bar{\mathbf{G}} - \bar{\mathbf{G}}^\mathsf{T}\bar{\mathbf{B}}\boldsymbol{\Gamma}\bar{\mathbf{B}}^\mathsf{T}\bar{\mathbf{G}})^{-1}(\bar{\mathbf{G}}^\mathsf{T} - \bar{\mathbf{G}}^\mathsf{T}\bar{\mathbf{B}}\boldsymbol{\Gamma}\bar{\mathbf{B}}^\mathsf{T})\bar{\boldsymbol{b}}
$$

$$
= (\bar{\mathbf{G}}^\mathsf{T}(\mathbf{I} - \bar{\mathbf{B}}\boldsymbol{\Gamma}\bar{\mathbf{B}}^\mathsf{T})\bar{\mathbf{G}})^{-1}\bar{\mathbf{G}}^\mathsf{T}(\mathbf{I} - \bar{\mathbf{B}}\boldsymbol{\Gamma}\bar{\mathbf{B}}^\mathsf{T})\bar{\boldsymbol{b}},
$$

where $(\mathbf{I} - \bar{\mathbf{B}}\boldsymbol{\Gamma}\bar{\mathbf{B}}^\mathsf{T})$ is a projection matrix. The above equation can be rewritten as,

$$
\boldsymbol{r}_{r,\mathrm{err}} = (\tilde{\mathbf{G}}^\mathsf{T}\tilde{\mathbf{G}})^{-1}\tilde{\mathbf{G}}^\mathsf{T}\bar{\boldsymbol{b}},
$$

where $\tilde{\mathbf{G}} \triangleq (\mathbf{I} - \bar{\mathbf{B}}\boldsymbol{\Gamma}\bar{\mathbf{B}}^\mathsf{T})\bar{\mathbf{G}}$.

Appendix B

Change in GNSS Satellite

Geometry

This appendix provides an approximation of the change in satellite geometry as a function of time. For a conservative approximation, the GNSS satellite is assumed to start at zenith, where the angular velocity from the surface of earth is fastest. GNSS satellites are in periodic orbits, returning to the same location over earth after T_{GNSS}. For example, $T_{\text{GNSS}} \approx 23$ hours, 56 minutes (i.e., 1436 minutes). Therefore, the amount of time it takes for the GPS satellite to travel ϕ degrees from the center of earth is given by

$$\text{Time for satellite to travel} = \frac{\phi \times 1436}{360\,^{\circ}}. \tag{B.1}$$

Using law of sines, ϕ can be expressed in terms of θ (the angle from zenith to the later satellite position from the earth surface) as follows

$$\phi = \theta - \arcsin\left(\frac{\sin(180\,^{\circ} - \theta)r_{\text{earth}}}{r_{\text{MEO}}}\right), \tag{B.2}$$

where r_{earth} is the radius of earth, and r_{MEO} is the radius of the middle earth orbit (MEO).

Equations (B.1) and (B.2) can be combined to calculate the time it takes for the satellite to travel θ degrees (see Fig. B.1).
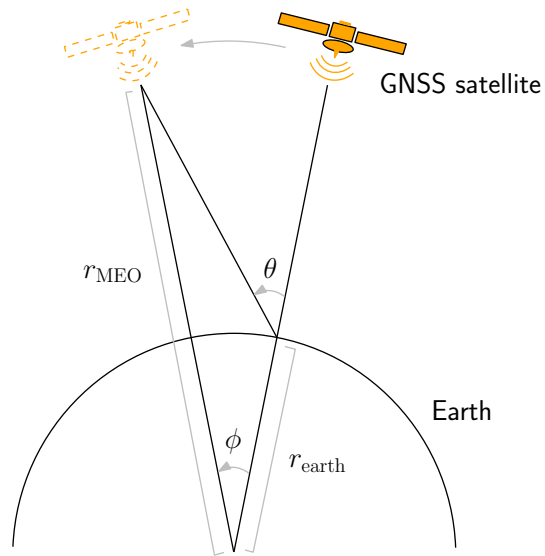

Figure B.1: Description of the variables used to approximate the change in satellite geometry.

Bibliography

[1] 46 corporations working on autnonomous vehicles. https://www.cbinsights.com/research/autonomous-driverless-vehicles-corporations-list/.

[2] Downtown buildings. https://services.arcgis.com/Fu2oOWg1Aw7azh41/arcgis/rest/services/DowntownBuildings/FeatureServer.

[3] Esri. https://www.arcgis.com.

[4] GNSS Radar. http://www.taroz.net/GNSS-Radar.html.

[5] Laird phantom 3G/4G multiband antenna nmo mount white TRA6927M3NB. https://www.lairdtech.com/products/phantom-series-antennas.

[6] National instrument universal software radio peripheral-2954R. http://www.ni.com/en-us/support/model.usrp-2954.html.

[7] Open Street Map foundation (OSMF). https://www.openstreetmap.org.

[8] Pyephem. https://rhodesmill.org/pyephem/.

[9] Remcom. https://www.remcom.com.

[10] Self-driving car accidents will keep happening. we need to learn from them. https://money.cnn.com/2018/03/21/technology/self-driving-cars-opinion/index.html?sr=fbmoney032118self-driving-cars-opinion0631AMStory.

[11] 3GPP. Evolved universal terrestrial radio access (E-UTRA); requirements for support of radio resource management. TS 36.133, 3rd Generation Partnership Project (3GPP), April.

[12] S. Bopardikar, B. Englot, A. Speranzon, and J. Berg. Robust belief space planning under intermittent sensing via a maximum eigenvalue-based bound. *The International Journal of Robotics Research*, 28:1609–1626, July 2016.

[13] J. del Peral-Rosado, J. Lopez-Salcedo, G. Seco-Granados, F. Zanier, and M. Crisci. Evaluation of the LTE positioning capabilities under typical multipath channels. In *Proceedings of Advanced Satellite Multimedia Systems Conference and Signal Processing for Space Communications Workshop*, pages 3992–3997, April 2012.

[14] E. Dijkstra. A note on two problems in connexion with graphs. *Numerische Mathematik*, 1(1):269–271, December 1959.

[15] European GSC. Galileo open service signal in space interface control document (OS SIS ICD). https://www.gsc-europa.eu/electronic-library/programme-reference-documents, December 2016.

[16] GPS World. Mitigation through adaptive filtering for machine automation applications. gpsworld.com/gnss-systemalgorithms-methodsinnovation-multipath-minimization-method-11849/, July 2011.

[17] P. Hart, N. Nilsson, and B. Raphael. A formal basis for the heuristic determination of minimum cost paths. *IEEE Transactions on Systems Science and Cypernetics*, 4(2):100–107, July 1968.

[18] L. Heng, T. Walter, P. Enge, and G. Gao. GNSS multipath and jamming mitigation using high-mask-angle antennas and multiple constellations. *IEEE Transactions on Intelligent Transportation Systems*, 16(2):741–750, April 2015.

[19] M. Huang and W. Xu. Enhanced LTE TOA/OTDOA estimation with first arriving path detection. In *Proceedings of IEEE Wireless Communications and Networking Conference*, pages 3992–3997, April 2013.

[20] C. Hubmann, J. Schulz, M. Becker, D. Althoff, and C. Stiller. Automated driving in uncertain environments: Planning with interaction and uncertain maneuver prediction. *IEEE Transactions on Intelligent Vehicles*, 3(1):5–17, March 2018.

[21] Inside GNSS. Multipath vs. NLOS signals. insidegnss.com/multipath-vs-nlos-signals/, November 2013.

[22] N. Jardak, A. Vervisch-Picois, and N. Samama. Multipath insensitive delay lock loop in GNSS receivers. *IEEE Transactions on Aerospace and Electronic Systems*, 47(4):2590–2609, October 2011.

[23] E. Kaplan and C. Hegarty. *Understanding GPS: Principles and Applications*. Artech House, second edition, 2005.

[24] H. Karimi and D. Asavasuthirakul. A novel optimal routing for navigation systems-services based on global navigation satellite system quality of service. *Journal of Intelligent Transportation Systems*, 18(3):286–298, May 2014.

[25] Z. Kassas, A. Arapostathis, and T. Humphreys. Greedy motion planning for simultaneous signal landscape mapping and receiver localization. *IEEE Journal of Selected Topics in Signal Processing*, 9(2):247–258, March 2015.

[26] Z. Kassas, V. Ghadiok, and T. Humphreys. Adaptive estimation of signals of opportunity. In *Proceedings of ION GNSS Conference*, pages 1679–1689, September 2014.

[27] Z. Kassas and T. Humphreys. Motion planning for optimal information gathering in opportunistic navigation systems. In *Proceedings of AIAA Guidance, Navigation, and Control Conference*, pages 4551–4565, August 2013.

[28] Z. Kassas and T. Humphreys. The price of anarchy in active signal landscape map building. In *Proceedings of IEEE Global Conference on Signal and Information Processing*, pages 165–168, December 2013.

[29] Z. Kassas and T. Humphreys. Observability analysis of collaborative opportunistic navigation with pseudorange measurements. *IEEE Transactions on Intelligent Transportation Systems*, 15(1):260–273, February 2014.

[30] Z. Kassas and T. Humphreys. Receding horizon trajectory optimization in opportunistic navigation environments. *IEEE Transactions on Aerospace and Electronic Systems*, 51(2):866–877, April 2015.

[31] Z. Kassas, J. Khalife, K. Shamaei, and J. Morales. I hear, therefore I know where I am: Compensating for GNSS limitations with cellular signals. *IEEE Signal Processing Magazine*, pages 111–124, September 2017.

[32] S. Kay. *Fundamentals of Statistical Signal Processing: Estimation Theory*. Prentice-Hall, Upper Saddle River, NJ, 1993.

[33] N. Kbayer and M. Sahmoudi. Performances analysis of GNSS NLOS bias correction in urban environment using a three-dimensional city model and GNSS simulator. *IEEE Transactions on Aerospace and Electronic Systems*, 54(4):1799–1814, February 2018.

[34] J. Khalife and Z. Kassas. Evaluation of relative clock stability in cellular networks. In *Proceedings of ION GNSS Conference*, pages 2554–2559, September 2017.

[35] J. Khalife and Z. Kassas. Precise UAV navigation with cellular carrier phase measurements. In *Proceedings of IEEE/ION Position, Location, and Navigation Symposium*, pages 978–989, April 2018.

[36] J. Khalife, S. Ragothaman, and Z. Kassas. Pose estimation with lidar odometry and cellular pseudoranges. In *Proceedings of IEEE Intelligent Vehicles Symposium*, pages 1722–1727, June 2017.

[37] Y. Lee, Y. Suh, and R. Shibasaki. Ajax GIS application for GNSS availability simulation. *Journal of Civil Engineering*, 11(6):303–310, November 2007.

[38] J. Lesouple, T. Robert, M. Sahmoudi, J. Tourneret, and W. Vigneau. Multipath mitigation for GNSS positioning in an urban environment using sparse estimation. *IEEE Transactions on Intelligent Transportation Systems*, pages 1–13, July 2018.

[39] M. Maaref, J. Khalife, and Z. Kassas. Lane-level localization and mapping in GNSS-challenged environments by fusing lidar data and cellular pseudoranges. *IEEE Transactions on Intelligent Vehicles*, 2018. accepted.

[40] Z. Meng, H. Qin, Z. Chen, X. Chen, H. Sun, F. Lin, and M. Jr. A two-stage optimized next-view planning framework for 3-D unknown environment exploration, and structural reconstruction. *IEEE Robotics and Automation Letters*, 2(3):1680–1687, July 2017.

[41] P. Misra and P. Enge. *Global Positioning System: Signals, Measurements, and Performance*. Ganga-Jamuna Press, second edition, 2010.

[42] M. Mora and J. Tornero. Predictive and multirate sensor-based planning under uncertainty. *IEEE Transactions on Intelligent Vehicles*, 16(3):1493–1504, June 2015.

[43] J. Morales and Z. Kassas. Optimal collaboraive mapping of terrestrial transmitters: Receiver placement and performance characterization. *IEEE Transactions on Aerospace and Electronic Systems*, 54(2):992–1007, April 2018.

[44] J. Morales, J. Khalife, A. Abdallah, C. Ardito, and Z. Kassas. Inertial navigation system aiding with Orbcomm LEO satellite Doppler measurements. In *Proceedings of ION GNSS Conference*, September 2018. accepted.

[45] Navstar GPS. Space segment/navigation user interfaces interface specification IS-GPS-200. http://www.gps.gov/technical/icwg/, December 2015.

[46] A. Nowak. Dynamic GNSS mission planning using DTM for precise navigation of autonomous vehicles. *Journal of Navigation*, pages 483–504, May 2017.

[47] K. Pesyna, Z. Kassas, J. Bhatti, and T. Humphreys. Tightly-coupled opportunistic navigation for deep urban and indoor positioning. In *Proceedings of ION GNSS Conference*, pages 3605–3617, September 2011.

[48] S. Ponda, R. Kolacinski, and E. Frazzoli. Trajectory optimization for target localization using small unmanned aerial vehicles. In *Proceedings of AIAA Guidance, Navigation, and Control Conference*, pages 6015–6040, August 2009.

[49] J. Ray, M. Cannon, and P. Fenton. GPS code and carrier multipath mitigation using a multiantenna system. *IEEE Transactions on Aerospace and Electronic Systems*, 37(1):183–195, January 2001.

[50] D. Roongpiboonsopit and H. Karimi. Integrated GNSS QoS prediction for navigation services. In *Proceedings of ACM SIGSPATIAL International Workshop on Computational Transportation Science*, pages 73–78, November 2013.

[51] S. Saab and Z. Kassas. Map-based land vehicle navigation system with DGPS. In *Proceedings of IEEE Intelligent Vehicle Symposium*, volume 1, pages 209–214, June 2002.

[52] S. Saab and Z. Kassas. Power matching approach for GPS coverage extension. *IEEE Transactions on Intelligent Transportation Systems*, 7(2):156–166, June 2006.

[53] K. Shamaei and Z. Kassas. LTE receiver design and multipath analysis for navigation in urban environments. *NAVIGATION, Journal of the Institute of Navigation*, 2018. accepted.

[54] K. Shamaei, J. Khalife, S. Bhattacharya, and Z. Kassas. Computationally efficient receiver design for mitigating multipath for positioning with LTE signals. In *Proceedings of ION GNSS Conference*, pages 3751–3760, September 2017.

[55] K. Shamaei, J. Khalife, and Z. Kassas. Comparative results for positioning with secondary synchronization signal versus cell specific reference signal in LTE systems. In *Proceedings of ION International Technical Meeting Conference*, pages 1256–1268, January 2017.

[56] K. Shamaei, J. Khalife, and Z. Kassas. Exploiting LTE signals for navigation: theory to implementation. *IEEE Transactions on Wireless Communications*, 17(4):2173–2189, April 2018.

[57] K. Shamaei, J. Khalife, and Z. Kassas. Pseudorange and multipath analysis of positioning with LTE secondary synchronization signals. In *Proceedings of Wireless Communications and Networking Conference*, pages 286–291, 2018.

[58] K. Shamaei, J. Morales, and Z. Kassas. Positioning performance of LTE signals in Rician fading environments exploiting antenna motion. In *Proceedings of ION GNSS Conference*, pages 3423–3432, September 2018.

[59] O. Gnana Swathika and S. Hemamalini. Prims-aided Dijkstra algorithm for adaptive protection in microgrids. *IEEE Journal of Emerging and Selected Topics in Power Electronics*, 4(4):1279–1286, December 2016.

[60] Z. Tang and U. Ozguner. Motion planning for multitarget surveillance with mobile sensor agents. *IEEE Transactions on Robotics*, 21(5):898–908, October 2005.

[61] D. Uciński. *Optimal Measurement Methods for Distributed Parameter System Identification*. CRC Press, 2005.

[62] R. Valencia, M. Morta, J. Andrade-Cetto, and J. Porta. Planning reliable paths with pose SLAM. *IEEE Transactions on Robotics*, 29(4):1050–1059, August 2013.

[63] D. H. Won, J. Ahn, S. Lee, J. Lee, S. Sung, H. Park, J. Park, and Y. J. Lee. Weighted DOP with consideration on elevation-dependent range errors of GNSS satellites. *IEEE Transactions on Instrumentation and Measurement*, 61(12):3241–3250, December 2012.

[64] J. Wu and A. Dempster. "BOC-gated-PRN" a multipath mitigation technique for BOC(n,n) waveforms. *IEEE Transactions on Aerospace and Electronic Systems*, 47(2):1136–1153, April 2011.

[65] B. Yang, K. Letaief, R. Cheng, and Z. Cao. Timing recovery for OFDM transmission. *IEEE Journal on Selected Areas in Communications*, 18(11):2278–2291, November 2000.

[66] H. Yu, K. Meier, M. Argyle, and R. Beard. Cooperative path planning for target tracking in urban environments using unmanned air and ground vehicles. *IEEE/ASME Transactions on Mechatronics*, 20(2):541–552, April 2015.

[67] Yujin and G. Xiaoxue. Optimal route planning of parking lot based on Dijkstra algorithm. In *Proceedings of the Robots Intelligent System Conference*, pages 221–224, October 2017.

[68] J. Zhang, Y. Feng, F. Shi, G. Wang, B. Ma, R. Li, and X. Jia. Vehicle routing in urban areas based on the oil consumption weight-Dijkstra algorithm. *IET Intelligent Transport Systems*, 10(7):495–502, September 2016.

[69] N. Ziedan. Urban positioning accuracy enhancement utilizing 3-D buildings model and accelerated ray tracing algorithm. In *Proceedings of the Technical Meeting of The Satellite Division of the Institute of Navigation*, pages 3253–3268, September 2017.